Research Square

Preprints are preliminary reports that have not undergone peer review.
They should not be considered conclusive, used to inform clinical practice,
or referenced by the media as validated information.

FDTD-Based Synthetic Dataset Generation and Quantum Ensemble Learning for Enhanced Microwave Tumor Localization

Muhammad Saood Sarwar

muhammad.saood@seecs.edu.pk

National University of Sciences and Technology

Shahzaib Ur Rehman

National University of Computer and Emerging Sciences

Research Article

Keywords: Microwave Imaging, FDTD Simulation, MEEP, Quantum Multi-Encoder Fusion Classifier (QMEFC), Hybrid Quantum Spatial Residual Network (HQ-SRN), Quantum Machine Learning, Dempster-Shafer Fusion, SVM.

Posted Date: August 14th, 2026

DOI: https://doi.org/10.21203/rs.3.rs-9634474/v1

License: This work is licensed under a Creative Commons Attribution 4.0 International License.
Read Full License

Additional Declarations: No competing interests reported.

FDTD-Based Synthetic Dataset Generation and Quantum Ensemble Learning for Enhanced Microwave Tumor Localization

Muhammad Saood Sarwar[1*] and Shahzaib Ur Rehman[2†]

[1*]School of Electrical Engineering and Computer Science(SEECS), National University of Sciences & Technology (NUST), H-12, Islamabad, 44000,Pakistan.

[2]Department of Computer Science, National University of Computer and Emerging Sciences - FAST, Phase 1 Hayatabad, Peshawar, 25100, Khyber Pakhtunkhwa, Pakistan.

*Corresponding author(s). E-mail(s): muhammad.saood@seecs.edu.pk;
Contributing authors: p248001@pwr.nu.edu.pk;
†These authors contributed equally to this work.

Abstract

Microwave-based tumor localization is a new non-invasive diagnostic tool that uses the differences in dielectric properties between healthy and cancerous tissues. Tumor tissue has a high water content, which leads to notable reflections of electromagnetic waves at the boundary between tissue types. This makes microwave imaging an effective method for detection. However, creating robust classification algorithms is often challenging due to the scarcity of labeled clinical datasets. This research presents a framework for generating high-quality synthetic microwave scattering data through Finite-Difference Time-Domain (FDTD) simulations. Our approach employs a multi-static MIMO setup and a differential imaging technique to separate tumor-specific signals from complex biological backgrounds. We assess the performance of a traditional Support Vector Machine (SVM) alongside individual quantum models, specifically the Quantum Multi-Encoder Fusion Classifier (QMEFC) and the Hybrid Quantum Spatial Residual Network (HQ-SRN). To enhance diagnostic accuracy, this research introduces the Quantum-Powered Fusion Classifier Ensemble (QPFC-E), which integrates these models via Dempster-Shafer (DS) belief fusion and AUC-weighted trust parameters. Experimental results show that the QPFC-E achieves an overall accuracy of 87.00% and a Macro AUC-ROC of 0.9354.

Notably, the ensemble method achieves a high recall of 61.3% for difficult tumor types, a substantial improvement over the classical baseline. This work demonstrates the potential of hybrid FDTD-QML frameworks in improving the accuracy of microwave diagnostics.

Keywords: Microwave Imaging, FDTD Simulation, MEEP, Quantum Multi-Encoder Fusion Classifier (QMEFC), Hybrid Quantum Spatial Residual Network (HQ-SRN), Quantum Machine Learning, Dempster-Shafer Fusion, SVM.

1 Introduction

1.1 Microwave Imaging for Tumor Detection

Early detection of tumors, especially breast and skin cancer, is crucial to lowering patient death rates [1, 2]. Rapid diagnosis of these cancers allows for less invasive treatments and greatly improves long-term survival rates [3–5]. However, the success of early screening depends a lot on the availability and precision of diagnostic imaging tools [6, 7].

Typical imaging methods, such as X-ray mammography, Computed Tomography (CT), and Magnetic Resonance Imaging (MRI), are the current clinical standards [8–10]. Although widely used, these techniques have clear limitations. X-rays and CT scans expose patients to ionizing radiation, which can be harmful with frequent use [11–14]. In addition, MRI systems are expensive to operate and need specialized facilities, making them difficult to access in areas with limited resources [15].

Microwave imaging has emerged as a promising alternative that solves many of these issues [16]. This technology does not use ionizing radiation and employs low-power electromagnetic waves [17], making it safe for repeated clinical use. One of its main benefits is the significant difference in dielectric properties between healthy and cancerous tissues. Tumors, which have a high water content, exhibit varying permittivity and conductivity compared to healthy fat or skin [18, 19]. As a result, electromagnetic waves reflect more strongly at tumor boundaries, creating a distinct physical signature that can be captured and analyzed with computational methods [20].

1.2 Challenges in Microwave Tumor Localization

Despite its potential, several major hurdles prevent microwave imaging from reaching its full clinical capability. One of the biggest challenges is the extreme lack of labeled clinical data [21]. Training strong machine learning models requires large and diverse datasets that include various tumor sizes, shapes, and locations [22]. However, collecting such data from human subjects involves complex ethical approvals and high hardware costs, creating a bottleneck in algorithm development [23].

In addition, the human body is a highly varied environment for the propagation of electromagnetic waves [24]. As waves travel through different biological layers, such as skin, fat, and glandular tissue, they interact in complex ways, including multi-path

scattering, refraction, and dielectric absorption. A significant technical challenge is the skin-flash effect, where the large reflection at the skin-air interface hides the much weaker signals coming from a deep-seated tumor [25]. These factors lead to a low signal-to-noise ratio that makes detection difficult.

As a result, traditional imaging algorithms often have trouble resolving small or early-stage cancers [26]. There is a need for better signal processing and classification frameworks that can deal with these nonlinear wave interactions. Using high-dimensional feature extraction and modern computational methods, it becomes possible to pick out the subtle scattering signatures needed for accurate tumor localization.

1.3 Role of Synthetic Datasets and FDTD Simulations

Numerical modeling provides a practical solution to the issue of limited data in medical imaging. The FDTD method, used through open-source MIT Electromagnetic Equation Propagation (MEEP) software, enables the quick creation of large-scale synthetic datasets [27]. By simulating thousands of unique clinical scenarios, researchers can generate diverse training samples needed for modern machine learning processes. This method avoids the ethical and logistical issues typically associated with human clinical trials in the early stages of algorithm development.

Unlike analytical path-loss approximations, the FDTD approach solves Maxwell's equations on a discretized grid [28]. This ability is crucial for capturing complex, real-world wave interactions like multi-path scattering, refraction at different tissue boundaries, and dielectric absorption. These simulations offer a high level of physical realism, ensuring that the synthetic data mirrors how electromagnetic waves behave in a multi-layered biological environment [29]. This detail is essential for training models that can later work with physical hardware.

To improve the detection of deep-seated tumors, this research uses the technique of differential imaging. This method creates two separate simulation states: a baseline that shows healthy tissue and a target state that includes a tumor. By subtracting the electromagnetic fields of these two states in a vector format, the main background reflections from the skin-fat interface are eliminated. This step effectively isolates subtle scattering signatures caused only by the tumor. The resulting differential signal provides a much clearer set of features, allowing classification models to concentrate on malignant signatures instead of the background anatomy.

1.4 Emergence of Quantum Machine Learning (QML)

QML brings together quantum computing and classical artificial intelligence in an exciting way. This field uses unique principles of quantum mechanics, like superposition [30] entanglement [31], to handle data in high-dimensional Hilbert spaces [32, 33]. One major benefit of QML is its ability to recognize patterns better than traditional algorithms [34]. By converting classical input features into quantum states, these models can find nonlinear relationships that are often too challenging for classical processors to solve [35].

This research is particularly useful for analyzing microwave scattering data. The signals from a multi-static MIMO array are complex and contain both magnitude and phase information that detail intricate wave interactions. Quantum states naturally fit into complex-valued vectors, allowing quantum circuits to effectively process electromagnetic signatures. Moreover, the high-dimensional mapping features of quantum kernels enable a more accurate separation between subtle tumor reflections and background noise. Consequently, QML provides a promising framework for improving the sensitivity and specificity of microwave-based medical diagnostics.

1.5 Contributions of This Research

The main goal of this research is to connect computational electromagnetics with quantum-enhanced signal processing for medical diagnostics. Here are the specific contributions of this work:

- This research presents a strong pipeline for generating synthetic microwave scattering datasets using the MEEP simulation engine. The framework automates the creation of complex biological environments and uses differential imaging to isolate tumor-specific signals from strong background reflections.
- The study offers a detailed comparison between classical baselines and several individual quantum models. This includes applying the QMEFC, the Variational Quantum Gate Classifier (VQGC), and the HQ-SRN to multi-static MIMO data.
- This work proposes a new QPFC-E. Unlike typical averaging methods, this framework uses DS belief fusion and AUC-weighted trust parameters to effectively combine predictions from multiple quantum models.
- The research shows that the proposed ensemble method greatly enhances the detection and differentiation of malignant neoplasms. The system achieves a high Macro AUC-ROC and successfully tackles the low-recall issues linked to difficult tumor classes that often overlap in the microwave spectrum.

Despite these advances, existing studies differ greatly in their modeling assumptions, data generation methods, and learning frameworks. This variety makes it difficult to evaluate their strengths and weaknesses. A detailed review of previous work is needed to place current approaches in context and pinpoint ongoing challenges.

2 Literature Review

This section looks at the evolution of microwave diagnostic techniques. Highlights the shift from traditional machine learning plateaus to quantum-enhanced architectures. It specifically explores how high-fidelity FDTD simulations and evidential fusion strategies tackle the ongoing issues of data scarcity and overlapping dielectric signatures in tumor localization.

A study in [36] looked at the community's heavy dependence on closed-source simulations and small sample sizes in breast microwave imaging (BMI). Introduced a large-scale open-access experimental dataset (UM-BMID) to create a standardized benchmark. The research used a pre-clinical air-operated bistatic microwave system to scan various 3D-printed, MRI-derived breast models. To show how useful the dataset

is, the researchers extracted features in the time domain through an inverse discrete Fourier transform and used them in a standard logistic regression classifier. In tests on a subset of 249 experimental phantom scans for a binary classification task (tumor-containing vs. healthy), the model achieved a baseline diagnostic accuracy of 85.00%. This demonstrates the potential of applying machine learning to microwave phantom data. However, the classification was limited to a straightforward binary outcome using a simple linear model, and measurements were limited to a single 2D vertical plane. This baseline confirms our basic dataset generation method, but strongly emphasizes the need for our QPFC-E.

This study in [37] examines the use of machine learning to automate the detection of breast lesions using clinical microwave data. It aims to provide a non-ionizing and non-invasive alternative to traditional mammography. The research used data from the MammoWave system, which measures complex frequency-domain signals through a rotating multi-bistatic antenna array. To handle high-dimensional clinical data, Principal Component Analysis (PCA) was used for feature extraction. A key part of the methodology involved the augmentation of the dataset with a Wasserstein Generative Adversarial Network with gradient penalty (WGANGP) to balance the representation of benign and malignant cases. A SVM with a Gaussian kernel was then used for the ternary classification, which includes no findings, benign, and malignant classes. While the model achieved a promising accuracy of 80.00% on the augmented dataset from a single hospital, cross-hospital testing on an independent dataset showed a sharp decline in performance, with accuracies between 29.00% and 44.00%. These findings highlight the challenges of overfitting to specific clinical sites and the difficulty of generalizing multi-class models in real-world situations. This research serves as an important benchmark for clinical performance, but the reported accuracy gap shows the need for better architectures.

This study [38] examines the clinical effectiveness of the SAFE (Scan and Find Early) microwave system to distinguish benign and malignant breast lesions. The research used a mechanically rotating bistatic antenna array that operates between 1 and 8 GHz to capture complex S_{21} scattering parameters. The real components of these frequency-domain signals served as input features for an Adaptive Boosting (AdaBoost) machine learning model. Tested on a clinical dataset of 113 patients (70 benign and 43 malignant), the model achieved an overall diagnostic accuracy of 78.00%. It had a sensitivity of 79.0% and a specificity of 77.0%. Although the framework performed well for larger lesions and younger groups of patients, its performance decreased in dense breast tissue with a sensitivity of 73.0%. These results show that raw microwave data can be used in clinical pathology, but also indicate a performance limit for traditional boost models. Our proposed framework QPFC-E, seeks to address these limits by using quantum fusion techniques.

The authors in [39] evaluated how useful deep learning architectures are for automated tumor detection using a large microwave sensing dataset. They used a Convolutional Neural Network (CNN) to process 2D sinograms created from absolute magnitude time-domain signals, which were converted from frequency-domain S-parameters. CNN was compared with a Dense Neural Network (DNN) and a traditional logistic regression classifier to see how well it extracted spatial features. The

study used the UM-BMID dataset, which includes 1257 experimental MRI-derived breast phantom scans, and applied data augmentation techniques, specifically horizontal reflection and translation, to improve training diversity. The results showed that CNN effectively utilized the inherent locality of the sinogram data, achieving an AUC-ROC between 78.0% and 90.0%. In contrast, the shallow learning and dense models struggled to generalize to unseen test data. However, the study noted that its performance was highly dependent on the vertical alignment of the tumor with the antenna plane and the volume of the phantoms. This dependence on specific spatial orientations points to a limitation in the classical generalization.

In this study [40], researchers developed a diagnostic framework that eliminates the need for radiation using the MammoWave system. This approach aims to overcome the issues of ionizing radiation and the discomfort patients experience with traditional mammography. The study used low-power radio-frequency signals within the 1- to 9 GHz range to capture backscattered complex signals S_{21} from 61 clinical breast cases. The researchers used an SVM classifier, testing various kernel functions. They found that combining a Gaussian kernel with 50 principal components (PCA) produced the most consistent results. The model reached a sensitivity of 84.40% and a specificity of 95.50% to distinguish breasts with radiological findings (WF) from those without findings (NF). However, the study pointed out that very small lesions (under 4 mm) often resembled healthy tissue, resulting in false-negative predictions. This clinical validation shows that microwave-based ML screening is feasible, but points out a specific challenge in identifying subtle, overlapping dielectric signatures. Our proposed QPFC-E builds on these results by using a trust-weighted quantum ensemble to target and clarify the uncertainty in these small malignant classes, with the goal of improving overall diagnostic accuracy.

This study [41] looks at how QML can classify breast cancer using Digital Breast Tomosynthesis (DBT) images. The aim is to offer a more efficient option than traditional transfer learning when medical datasets are small. The authors proposed a pipeline that combines a Quantum Kernel Support Vector Machine (QKSVM) with different quantum state encoding strategies, such as Angle, Instantaneous Quantum Polynomial (IQP), and Quantum Approximate Optimization Algorithm (QAOA) embeddings. The method extracts features using six different mathematical models and then reduces dimensions with Linear Discriminant Analysis (LDA) to create a significant 2D feature vector. Experimental results, tested on both the Statevector simulator and the Aspen-M-3 real-time quantum processor, showed that the Angle-embedding version of the QKSVM reached a maximum testing accuracy of 84.33%. Although the research confirms that quantum kernels can work well for high-dimensional clinical image analysis, a major limitation is the model's reliance on expert radiologists to manually crop the Region of Interest (ROI) for reliable results. This baseline performance indicates a limit for standalone quantum kernels in oncology. Motivates our proposed QPFC-E, which aims to increase diagnostic accuracy by combining different quantum perspectives.

Researchers introduced in [42] a Weighted Fuzzy Dempster Shafer (DS) framework to tackle the difficulties of handling conflicting and unclear evidence in multimodal information integration. The research method combined fuzzy set theory with the

traditional DS evidence framework. It used fuzzy membership functions to represent diagnostic uncertainty and assigned fixed weights to individual sensors based on their perceived reliability. When evaluated in multimodal medical imaging datasets, the framework showed a significant improvement over simple probabilistic fusion, achieving a diagnostic accuracy of approximately 81.50%. Although the fuzzy-weighted approach effectively manages the uncertainty of sensor inputs and reduces the impact of conflicting evidence, it is limited by the constraints of classical feature mapping and the need for manually defined fuzzy parameters. This research highlights the mathematical strength of evidential reasoning in medical AI, but the reported performance suggests a clear need for our proposed QPFC-E. By replacing traditional fuzzy inputs with high-dimensional quantum Hilbert space mappings and adding dynamic AUC-weighted trust parameters, this boosts the diagnostic accuracy.

This study [43] proposed an automated computerized method to classify breast tumors as benign or malignant using ultrasound imaging. The research involved extracting ten important handcrafted features from the region of interest (ROI). These features included circularity, solidity, and various texture metrics based on GLCM. The team used these features to create a relational graph, where individual images acted as nodes, and edges were defined by the Spearman correlation coefficient. The classification process used an optimized Graph Neural Network (GNN), which was improved through an extensive ablation study and Bayesian optimization. A significant innovation here was the use of correlation thresholding and cluster-based analysis to filter the graph. This approach effectively removed edge anomalies, such as weak connections between similar classes and strong connections between different classes. Upon evaluation of the BUSI dataset, the optimized GNN reached a diagnostic accuracy of 99.48% with a correlation threshold of 0.95. This result was a significant improvement over a baseline model that used the Histogram of Oriented Gradients (HOG) features and achieved 86.91% accuracy. Although the study shows outstanding results, it is limited by the relatively small dataset. This size may not capture the full range of tumor characteristics seen in different clinical environments. This research highlights the promise of graph-based structures in medical diagnostics. However, challenges related to generalizability and reliance on specific correlation thresholds drive our development of the QPFC-E.

3 Methodology: FDTD-Based Synthetic Dataset Generation

The synthetic data generation process is based on the FDTD method. This research uses MEEP software [44] to solve Maxwell's equations on a divided spatial grid. This method captures complex wave interactions, such as multi-path scattering and dielectric absorption, with high physical accuracy.

3.1 MEEP Environment and Simulation Setup

The simulation environment is configured to replicate a highly controlled 2D Cartesian grid. The following sections define the spatial constraints and the mathematical formulation of the simulation domain.

3.1.1 Dimensionality and Domain Boundaries

The FDTD engine models a transverse slice of biological tissue within a two-dimensional space. To simulate an open-boundary environment and prevent artificial reflections, the simulation cell is enclosed by Perfectly Matched Layers (PML). The thickness and placement of these layers are governed by the parameters defined in Table 1.

Table 1 Boundary and Simulation Configuration Parameters

Parameter	Symbol	Value
PML Thickness	d_{pml}	2.0 mm
PML Padding Buffer	p_{pad}	2.0 mm
Center Frequency	f_c	6.0 GHz
Minimum Resolution	R	20 pixels/unit

A specific padding buffer, p_{pad}, is integrated between the antenna plane and the upper PML boundary. This buffer prevents numerical artifacts from prematurely dampening the emitting sources and ensures the preservation of the near-field signal characteristics before they interact with the tissue layers.

3.1.2 Grid Size Formulation and Resolution

The spatial dimensions of the simulation domain are dynamically calculated to accommodate the transmitter-receiver array and the varying depths of biological tissue. The total width (W_{domain}) and depth (D_{domain}) of the simulation grid are determined by the following equations:

$$W_{domain} = (N_{rx} + 8) \times S + 2d_{pml} \tag{1}$$

$$D_{domain} = 2d_{pml} + p_{pad} + L_{max} + T_{max} + 10.0\,\text{mm} \tag{2}$$

In Equation 1, N_{rx} represents the number of receivers and S denotes the spatial interval between them. In Equation 2, L_{max} and T_{max} represent the maximum cumulative depth of the biological layers and the target tumor, respectively. An additional 10.0 mm margin is maintained to allow complete wave propagation beyond the target region.

To maintain numerical stability and prevent spatial aliasing, grid resolution (R) must satisfy the Courant–Friedrichs–Lewy (CFL) stability bounds. The discretization limit is established as:

$$R \geq 20 \quad \text{[pixels per MEEP unit]} \tag{3}$$

This resolution ensures that the spatial step size is sufficiently small to resolve the shortest wavelengths present within high-permittivity biological tissues, thereby ensuring the accuracy of the extracted scattering signatures.

3.2 Source Injection and Frequency Normalization

The simulation utilizes dimensionless units to maintain scale-invariance within the FDTD engine. Consequently, physical SI units must be normalized before execution to ensure accurate wave-tissue interactions.

3.2.1 Center Frequency and Unit Normalization

The center frequency of the simulation is governed by the MEEP unit length scale, L_{meep}, and the speed of light in a vacuum, c. To convert the real-world frequency (f_{Hz}) into the simulation frequency (f_{meep}), the normalization formula is applied using Equation 4.

$$f_{meep} = \frac{f_{Hz} \cdot L_{meep}}{c} \tag{4}$$

In this study, f_{Hz} is established at 6.0 GHz. The normalization process ensures that the temporal and spatial steps within the discretized grid remain consistent with the physical properties of the electromagnetic wave.

3.2.2 Pulse Dynamics and Bandwidth

To simulate the broadband response typical of physical horn or patch antennas, transmitters are configured to emit Gaussian pulses. The temporal profile of the source is defined by a center frequency f_{meep} and a fractional frequency width parameter, Δf. Using Equation 5, the bandwidth is configured to 10% of the center frequency to provide a robust spectral coverage for the tumor localization task.

$$\Delta f = 0.10 \times f_{meep} \tag{5}$$

The use of a broadband Gaussian source allows for the extraction of multi-static features across a range of frequencies, though the primary diagnostic data is extracted at the center incidence for this research.

3.2.3 Source Polarization

The signal injection is restricted to a single vector component to maintain computational efficiency and simplify the scattering analysis. The electric field in Equation 6 is polarized exclusively along the Z-axis, corresponding to the transversal electric (TE) mode in a 2D Cartesian plane.

$$\mathbf{E}(\mathbf{r}, t) = E_z(\mathbf{r}, t)\hat{\mathbf{k}} \tag{6}$$

By utilizing the E_z component, the simulation captures the essential scattering and diffraction patterns resulting from the interaction between the incident wave and the heterogeneous tissue boundaries.

3.3 Dielectric Tissue Formatting and Material Conversion

The physical realism of the FDTD simulation depends on the accurate representation of biological tissues. In the MEEP environment, these tissues are defined by their geometric bounds and their corresponding complex dielectric properties.

3.3.1 Stratified Tissue Layers

To simulate a realistic anatomical profile, the biological environment is constructed using a stratified layer approach. The healthy tissue model consists of four distinct layers: the epidermis, dermis, skin-fat interface, and a primary fat layer. Each layer is represented as a rectangular geometric volume with a specific thickness and relative permittivity (ϵ_r). These layers are arranged sequentially along the Y-axis to replicate the depth-dependent dielectric variations found in human tissue. The thicknesses of these layers are randomized within clinical bounds to ensure the diversity and robustness of the resulting dataset.

3.3.2 Tumor Modeling

Malignant formations are integrated into the simulation as target objects within the fat layer. These tumors are modeled as cylindrical geometric structures, characterized by a specific radius and spatial coordinates (x, y). To replicate the biological properties of cancerous tissue, these cylinders are assigned significantly elevated permittivity and conductivity values compared to the surrounding healthy environment. This dielectric contrast is the primary driver of the scattering signatures captured by the receiver array.

3.3.3 SI to MEEP D-Conductivity Conversion

While permittivity values map directly into the MEEP environment, conductivity values (σ) require a mathematical conversion. MEEP utilizes a dimensionless D-conductivity parameter to account for dielectric absorption. To ensure that the clinical SI units (S/m) result in identical wave behavior within the simulation, the exact conversion formula is applied using Equation 7.

$$\sigma_{meep} = \frac{\sigma_{SI} \cdot L_{meep}}{c \cdot \epsilon_r \cdot \epsilon_0 \cdot 2\pi} \tag{7}$$

Where:

- σ_{SI} is the real-world conductivity in Siemens per meter (S/m).
- L_{meep} is the MEEP unit length scale.
- c is the speed of light in a vacuum.
- ϵ_r is the relative permittivity of the specific tissue layer.
- ϵ_0 is the vacuum permittivity.
- 2π is the frequency normalization factor.

This normalization ensures that the spatial dielectric absorption within the simulation accurately represents the energy loss observed in real-world biological tissues at the center frequency of 6.0 GHz.

3.4 Execution Phase: Transmit-Receive (Tx/Rx) Polling

The execution phase is designed to extract high-dimensional scattering data through a systematic polling sequence. This process is divided into two topological state instances to facilitate the isolation of tumor-specific features.

3.4.1 Differential Imaging Principle

To effectively isolate the scattering influences of a malignancy, the simulation follows a differential imaging framework. Each observation scenario involves two separate simulation runs:

1. **Baseline Generation (G_h):** The simulation grid is populated strictly with healthy biological tissue layers. This run captures the primary reflections from the skin-air and skin-fat interfaces.
2. **Target Generation (G_u):** The simulation is re-executed with the exact same boundary and tissue parameters, but with the inclusion of highly dielectric tumor cylinders.

By maintaining identical grid geometries and source characteristics across both instances, the subsequent subtraction of the electromagnetic fields allows for the total cancellation of the skin-flash effect and other background artifacts.

3.4.2 Multi-Static MIMO Configuration

The signal acquisition follows a multi-static Multiple-Input Multiple-Output (MIMO) configuration. The array consists of $N_{tx} = 4$ transmitters and $N_{rx} = 16$ receivers. The transmitters are positioned along the skin surface to span the lateral width of the tissue, while the receivers are arranged in a uniform linear array.

The system operates iteratively; a single transmitter $Tx(i)$ fires a Gaussian burst, and the resulting field fluctuations are recorded simultaneously across all sixteen receiver positions $Rx(j)$. This iterative polling results in a total of 64 independent spatial channels per simulation state, providing a comprehensive spatial map of the internal scattering environment.

3.4.3 Temporal Signal Acquisition and DFT Monitoring

The temporal dynamics of the simulation are governed by the traversal time required for the electromagnetic wave to propagate through the tissue and reflect back to the antenna plane. To ensure that all secondary and tertiary reflections are captured, the simulation runtime (t_{total}) in Equation 8 is bounded by the spatial depth of the cell.

$$t_{total} \approx 4 \times \frac{D_{domain}}{c_{avg}} \tag{8}$$

Where c_{avg} represents the average effective phase velocity within the heterogeneous medium. During this interval, temporal electromagnetic field fluctuations are aggregated at every designated receiver point. Rather than storing the entire time-domain waveform, Discrete Fourier Transform (DFT) monitors are utilized to extract the complex-valued field components exclusively at the center incidence frequency, f_{meep}. This approach significantly reduces the data footprint while preserving the phase and magnitude information essential for quantum feature mapping.

3.5 Multi-Static Feature Extraction and Dataset Formulation

Following the completion of the FDTD simulation phases, the recorded electromagnetic fields undergo a post-processing sequence to isolate diagnostic information and format the data for machine learning.

3.5.1 Baseline Reflection Removal

The primary challenge in microwave-based tumor detection is the high-magnitude reflection occurring at the skin-fat interface, commonly referred to as the "skin-flash" effect. To resolve the significantly weaker scattering signals from deep-seated malignancies, a vector subtraction is performed between the target and baseline simulation states. The extracted differential signal, S_{ext}, is defined in Equation 9.

$$S_{ext} = S_{unhealthy} - S_{healthy} \tag{9}$$

$S_{unhealthy}$ represents the complex field components from the tumor-inclusive simulation, while $S_{healthy}$ represents the baseline response. This operation negates the dominant anatomical reflections, leaving a residual signal influenced primarily by the presence of the tumor.

3.5.2 Complex Feature Extraction

The diagnostic features are extracted from the Discrete Fourier Transform (DFT) monitors at the center frequency, f_c. For every transmitter-receiver pair, the system records a raw complex value representing the phase and magnitude of the scattered electric field. With a configuration of four transmitters ($N_{tx} = 4$) and sixteen receivers ($N_{rx} = 16$), each simulation sample yields a 4×16 multi-static matrix, resulting in 64 complex-valued data points per instance.

3.5.3 Empirical Noise Integration

To ensure the dataset remains resilient against hardware-derived imperfections and environmental interference, a static complex empirical thermal noise layer is integrated into the signals. A complex noise component with a magnitude of 10^{-6} is added to the extracted DFT values. This step bridges the gap between idealized numerical simulations and the stochastic nature of physical microwave measurement systems.

3.5.4 Dataset Structure and Feature Vectorization

The final dataset is compiled as a flattened feature vector that merges the multi-static MIMO signatures with the ground-truth geometric labels. The resulting matrix consists of 1,500 samples, each containing the following components:

- **Target Labels:** These include the tumor count, spatial coordinates, radius, relative permittivity, and conductivity values.
- **Tissue Parameters:** These consist of the skin offset, layer thicknesses (epidermis, dermis, fat), and the respective permittivity of each biological layer.

- **MIMO Features:** The 4×16 complex matrix is decomposed into its constituent real and imaginary parts. This results in 128 continuous numerical features, representing the complete set of transmitter-receiver combinations in the array.

3.5.5 Class Definitions

The classification task is categorized into three distinct states based on the physical characteristics of the simulation environment:

1. **Healthy:** Scenarios containing strictly stratified tissue layers without any malignant inclusions.
2. **T1:** Scenarios containing a single tumor at varying depths and sizes, characterized by specific dielectric properties.
3. **T2:** A secondary malignant class representing variations in tumor depth or dielectric intensity, utilized to test the discriminative limits of the classifiers.

4 Dataset Characterization and Statistical Analysis

To check the physical integrity of the synthetic FDTD dataset and evaluate the usefulness of the extracted features, a detailed statistical analysis was conducted. This initial phase confirms that the different scattering signatures are statistically significant and appropriate for quantum-based classification.

4.1 Dataset Composition and Overview

The generated dataset has 1,500 independent simulation samples. The class distribution is balanced to ensure the model includes both healthy physiological variations and a range of malignant scenarios. You can see the details in Table 2.

Table 2 Master Summary of the FDTD-Generated Dataset

Metric	Value
Total Samples	1,500
Total Features (MIMO)	128
Healthy Samples	500 (33.3%)
T1 Samples (Single Tumor)	400 (26.7%)
T2 Samples (Target Variants)	600 (40.0%)
MIMO Signal Range	[-8.62, 14.42]

The dataset includes 128 MIMO features that represent the real and imaginary parts of the backscattered electric field. The class distribution analysis in Figure 1 shows that the dataset adequately represents each class. This helps prevent majority-class bias during the training of the quantum architectures.

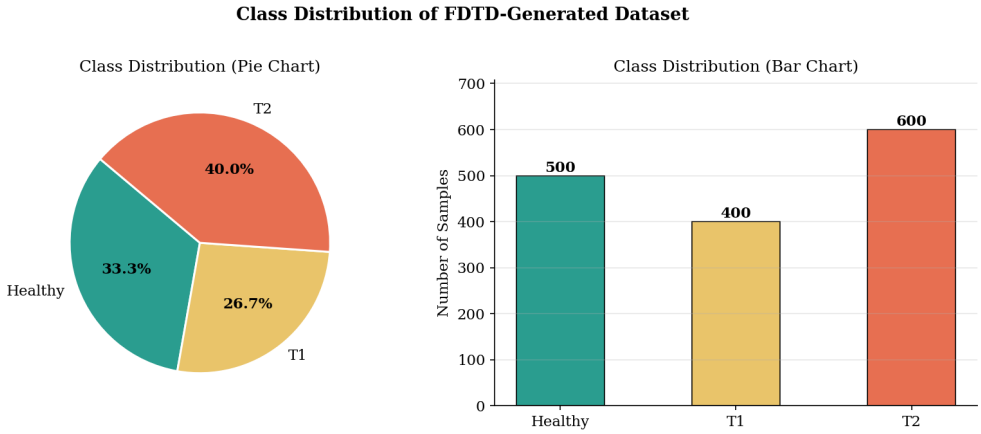


Fig. 1 Class distribution of the FDTD-generated dataset showing the balance between Healthy, T1, and T2 samples.

4.2 Signal Energy and Feature Sparsity

The differential signals show different energy profiles across the three classes. The L2 norm of the feature vectors represents the total backscattered energy. Statistical analysis shows a significant difference in magnitude: the Healthy class has a mean L2 norm of 34.25, while the T2 class has the lowest energy at 0.18. This difference is shown in Table 3.

Table 3 MIMO Differential Signal Statistics per Class

Class	Mean	Std. Dev	L2 Norm (Mean)	Sparsity
Healthy	0.2009	3.0223	34.25	0.4%
T1	-0.0005	0.3922	2.96	32.9%
T2	0.0001	0.0190	0.18	65.5%

The high sparsity (65.5%) in the T2 class shows that many MIMO channels record almost zero differential values for some tumor configurations. This creates a significant challenge for individual classifiers. The visual representation of these signal distributions (Figure 2) confirms that Healthy samples are widely spread out, while T1 and T2 signals are clustered closely around the origin.

4.3 Feature Importance and Statistical Significance

To confirm that the 128 MIMO channels have non-random, diagnostic information, we used the Kruskal-Wallis H-test on each feature. The results show that all 128 channels are highly statistically significant, with a p-value less than 0.001. As shown in Figure 3, the $-\log_{10}(p)$ values for all channels consistently go beyond the critical threshold. This confirms that each transmitter-receiver pair helps with class separability.

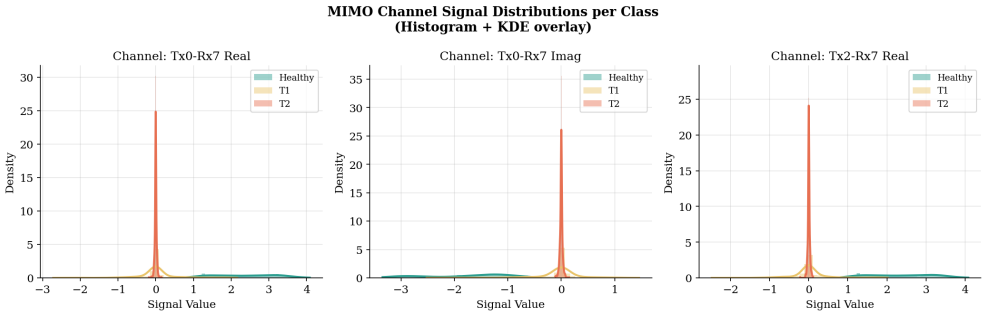


Fig. 2 MIMO channel signal distributions per class (Histogram + KDE overlay) illustrating the overlap and sparsity of malignant signatures.

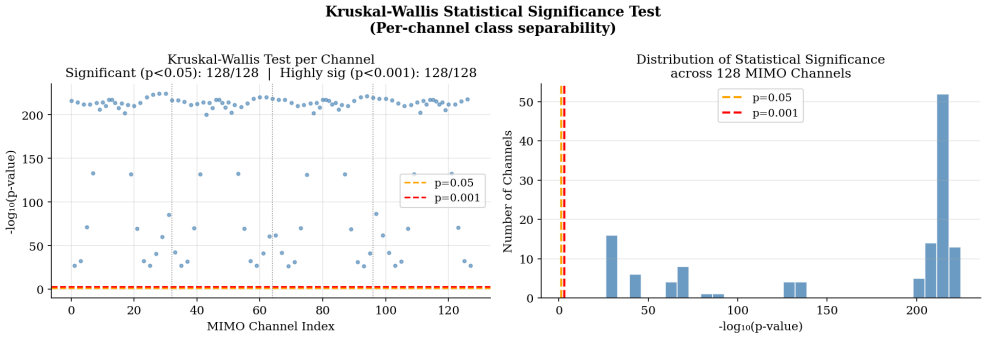


Fig. 3 Kruskal-Wallis statistical significance test demonstrating that all 128 MIMO channels provide highly significant class separability ($p < 0.001$).

4.4 Dimensionality Reduction and Separability Analysis

PCA was utilized to examine the variance structure of the MIMO features. The analysis indicates that 3 principal components account for 90% of the variance, while 5 components capture 95%. The PCA projections (Figure 4) reveal that the Healthy class forms a distinct, high-variance manifold. However, the T1 and T2 classes exhibit significant overlap in the reduced feature space.

The t-SNE embedding further clarifies this relationship, showing that tumor samples are clustered in a complex, nonlinear region of the feature space. This high degree of overlap between T1 and T2 justifies the move toward quantum-enhanced models and ensemble fusion strategies to resolve the subtle boundaries between malignant subtypes.

5 Methodology: QML Models and Fusion

The classification of complex microwave scattering signatures requires a robust interface between classical data and quantum computational states. This section details

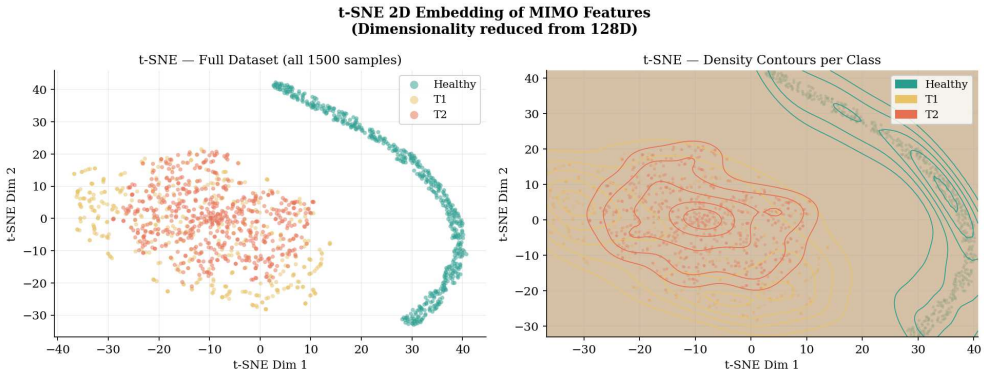


Fig. 4 Dimensionality reduction analysis: (Left) PCA projections of the first three components; (Right) t-SNE 2D embedding showing the nonlinear clustering of tumor subtypes.

the preprocessing pipeline, the individual quantum architectures, and the proposed ensemble fusion strategy.

5.1 Data Preprocessing for QML

Before introducing the synthetic dataset to the quantum circuits, the raw features must go through careful refinement. This step ensures numerical stability and compatibility with quantum state preparation techniques.

5.1.1 Feature Scaling and Dimensionality Reduction

The differential MIMO signals show different magnitudes based on the transmitter-receiver pair and the biological environment. To stop high-amplitude features from dominating the learning process, z-score normalization is applied to all 128 MIMO channels. Each feature, x, is changed into a scaled representation, z, using the equation 10.

$$z = \frac{x - \mu}{\sigma} \tag{10}$$

Where μ and σ represent the mean and standard deviation of the feature across the training set. After normalization, PCA is used to reduce the feature space from 128 dimensions to 16 principal components. This reduction is important for keeping computational efficiency in the quantum simulator while preserving over 95% of the total signal variance.

5.1.2 Quantum State Encoding

To process the scaled features in a quantum environment, the numerical data must be mapped into the amplitudes of a multi-qubit state. This study uses amplitude encoding, which is very efficient for high-dimensional microwave data [45]. For a given normalized feature vector $\mathbf{z}$, the corresponding quantum state $|\psi\rangle$ is prepared using Equation 11.

$$|\psi\rangle = \sum_{i=0}^{2^n-1} c_i |i\rangle \tag{11}$$

In this formulation, the normalized features are linked to the complex amplitudes c_i, so the total probability $\sum |c_i|^2$ equals one. This study uses a 4-qubit register to encode the 16 main components. Since the original MIMO data has both real and imaginary parts, this encoding method keeps the phase and size information of the scattering signatures intact during the quantum evolution process. This mapping lets the following quantum kernels and variational circuits work in a high-dimensional Hilbert space, where small differences between tumor classes can be better distinguished.

5.2 Classical Baseline Model: Radial Basis Function SVM

To establish a performance standard for the quantum architectures, a classical SVM with a Radial Basis Function (RBF) kernel is used. The SVM is a supervised learning method that finds the best hyperplane to separate different classes with the largest margin [46].

In microwave tumor localization, the link between backscattered signals and tumor features is nonlinear. The RBF kernel is especially suitable for this task because it lets the model map input features into a higher-dimensional space without needing manual feature engineering [47]. The RBF kernel function, $K(\mathbf{x}, \mathbf{x}')$, between two feature vectors $\mathbf{x}$ and $\mathbf{x}'$ is defined using Equation 12.

$$K(\mathbf{x}, \mathbf{x}') = \exp\left(-\gamma \|\mathbf{x} - \mathbf{x}'\|^2\right) \tag{12}$$

In Equation 12, the parameter γ controls how much individual training samples affect the decision boundary. For this research, the classical baseline is set with a regularization parameter of $C = 10$ and an adjusted γ. To address the three-class problem (Healthy, T1, and T2), we use a One-vs-Rest (OvR) strategy. This classical model serves as an important reference for evaluating whether quantum-enhanced feature mapping provides a real benefit in distinguishing between malignant sub-classes.

5.3 QK-SVM with SWAP-TEST

The QK-SVM is a step forward from traditional kernel methods [48]. It uses the high-dimensional Hilbert space of a quantum system for feature mapping. Rather than depending on a set classical function, the study uses a quantum circuit to find the similarity between samples. This approach can potentially identify nonlinear patterns that classical kernels cannot reach.

5.3.1 Quantum Feature Mapping

The QK-SVM process starts by mapping the 16 main components of the microwave scattering data into a quantum state. This research uses Amplitude Encoding, which shows a classical vector $\mathbf{x}$ as the coefficients of a quantum state $|\phi(\mathbf{x})\rangle$. A feature map achieves this mapping and requires n qubits to represent 2^n features. In the

current implementation, a 4-qubit register encodes the reduced MIMO feature set. This mapping allows the data to be processed in a complex-valued vector space, which naturally fits the phase and magnitude information found in electromagnetic signals.

5.3.2 Kernel Estimation via SWAP-TEST

To find the entries of the Gram matrix, the study uses the SWAP-TEST circuit. The SWAP-TEST is a basic quantum algorithm that measures the overlap, or inner product, between two quantum states, $|\phi(\mathbf{x}_i)\rangle$ and $|\phi(\mathbf{x}_j)\rangle$. The circuit uses an auxiliary ancilla qubit and two quantum registers, resulting in a total of 9 qubits for the computation. The probability of measuring the ancilla qubit in the $|0\rangle$ state relates to the state overlap, as shown in Equation 13.

$$P(0) = \frac{1}{2} + \frac{1}{2}|\langle\phi(\mathbf{x}_i)|\phi(\mathbf{x}_j)\rangle|^2 \tag{13}$$

The quantum kernel value, $K(\mathbf{x}_i, \mathbf{x}_j)$, is subsequently extracted by normalizing the measurement result:

$$K(\mathbf{x}_i, \mathbf{x}_j) = 2 \cdot P(0) - 1 = |\langle\phi(\mathbf{x}_i)|\phi(\mathbf{x}_j)\rangle|^2 \tag{14}$$

5.3.3 Quantum Kernel Matrix Analysis

The resulting quantum kernel matrix gives a high-dimensional similarity map of the dataset. Figure 5 shows that the Gram matrix for the training samples has a complex structure of inter-class similarities. The heat map displays the normalized overlap values. A value of 1.0 (represented in yellow) indicates identical quantum states.

The visual evidence of structured clusters in the kernel matrix suggests that the amplitude encoding and the following quantum evolution effectively distinguish the scattering profiles of healthy and malignant tissues. By using this quantum-calculated matrix, the SVM can find the best separating hyperplane within the quantum-enhanced feature space.

5.4 Variational Quantum Models

While Quantum Kernel methods focus on calculating state overlaps, Variational Quantum Circuits (VQCs) offer a different approach. VQCs use a hybrid framework where a parameterized quantum circuit is optimized repeatedly by a classical optimizer [49]. This study examines three different variational architectures designed for the complex nature of multi-static MIMO data.

5.4.1 VQGC

The VQGC presents a new method by representing the 4×16 MIMO matrix as a bipartite graph. In this setup, the transmitters (Tx) and receivers (Rx) act as separate nodes, while the complex scattering signals represent the edge weights.

To integrate this into a quantum environment, classical graph preprocessing is conducted first. The differential signal $S_{ij} = S_{ij}^{real} + iS_{ij}^{imag}$ defines the adjacency

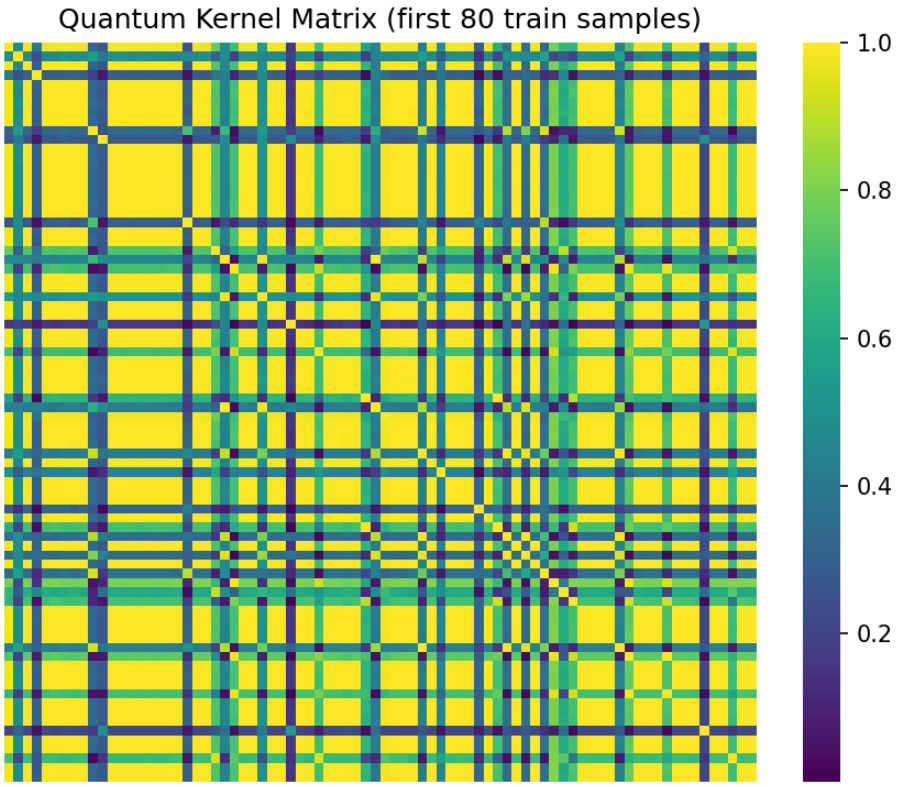


Fig. 5 Quantum Kernel Matrix generated via the SWAP-TEST circuit for the first 80 training samples. The intensity of the values represents the state overlap in the Hilbert space.

matrix $\mathbf{W}$. The edge weight is determined by the magnitude $|S_{ij}|$ and the phase by $\angle S_{ij}$. Specific features are extracted from the nodes, including the weighted degree and phase entropy for the transmitter nodes, and the peak response and spatial spread for the receiver nodes. This process creates a dense 8-dimensional graph-signal vector, $\mathbf{x}_{graph}$.

These features are angle-encoded into an 8-qubit circuit using a Quantum Approximate Optimization Algorithm (QAOA) inspired approach. The data is re-uploaded through multiple layers ($N_L = 5$) with R_y and R_z rotation gates. The main innovation of the VQGC is its entanglement strategy, which directly reflects the hardware's physical connections. The entanglement blocks perform Controlled-NOT (CNOT) operations across the bipartite gap ($Tx_i \leftrightarrow Rx_i$) and Controlled-$Z$ (CRZ) operations to create intra-layer rings among the transmitters and receivers. The final classification results are obtained by measuring the correlated Pauli-Z expectation values across the bipartite pairs using Equation 15.

$$E_k = \langle \psi(\mathbf{x}, \boldsymbol{\theta}) | \hat{Z}_k \otimes \hat{Z}_{k+4} | \psi(\mathbf{x}, \boldsymbol{\theta}) \rangle \tag{15}$$

Where $\boldsymbol{\theta}$ represents the trainable parameters. These expectation values are passed through a classical softmax function to yield the final class probabilities. The model is optimized using an Adam optimizer with a custom cross-entropy loss function.

5.4.2 QMEFC

The QMEFC is designed to handle the complex nature of electromagnetic scattering. Standard flat encoders often miss the relationship between the in-phase (real) and quadrature (imaginary) components of a signal. To keep this phase-magnitude connection, the QMEFC uses a dual-register quantum structure.

During preprocessing, the multi-static MIMO signals are divided into their real and imaginary matrices. Independent PCA simplifies each domain to eight main components. These two 8-dimensional vectors are then mapped into two separate 3-qubit registers (called Reg_A and Reg_B) using amplitude encoding, creating a 6-qubit system.

The quantum circuit has five parameterized layers. In each layer, it applies independent single-qubit rotations (R_x, R_y, R_z) and intra-register entangling rings (using CNOT gates) to find localized patterns in the real and imaginary domains separately. After that, a transversal fusion layer applies pairwise CNOT operations across the registers to entangle the real and imaginary states using Equation 16.

$$|\psi_{fusion}\rangle = \prod_{i=0}^{N-1} \text{CNOT}_{A_i,B_i} \left(|\psi_{real}(\mathbf{x}_{re}, \boldsymbol{\theta}_{re})\rangle \otimes |\psi_{imag}(\mathbf{x}_{im}, \boldsymbol{\theta}_{im})\rangle \right) \tag{16}$$

By delaying the entanglement until a higher-dimensional quantum state is established, the model preserves the delicate phase shifts caused by highly dielectric tumor tissues. The final classification features are extracted by measuring the joint correlation between the registers using tensor products of Pauli-Z observables:

$$E_k = \langle \psi_{fusion} | \hat{Z}_{A_k} \otimes \hat{Z}_{B_k} | \psi_{fusion} \rangle \tag{17}$$

These expectation values are processed via a classical softmax function to yield the final diagnostic probabilities.

5.4.3 HQ-SRN

The HQ-SRN combines the spatial feature extraction abilities of classical deep learning with the nonlinear high-dimensional mapping of quantum circuits. Multi-static MIMO arrays naturally generate spatially correlated data. Adjacent receivers capture similar diffraction patterns from a localized tumor.

To take advantage of this spatial continuity, the input data is organized as a 20-channel 1D spatial tensor across 16 receiver positions. This tensor captures the wave behavior by calculating the logarithmic magnitude, arctangent phase, and cross-transmitter differential signals. The classical part of the HQ-SRN uses a 1D Residual Network (ResNet) with Squeeze-and-Excitation (SE) attention blocks. This design works as a trainable spatial filter, learning which transmitter channels and feature types are most effective.

The classical convolutional layers reduce the spatial tensor to a 512-dimensional vector. Dense layers then compress this further into a 10-dimensional latent bottleneck vector. A hyperbolic tangent activation transforms these latent features into valid quantum rotation angles $[-\pi, \pi]$. Next, these features are used in a parameterized 10-qubit Data Re-uploading VQC according to Equation 18.

$$\hat{U}_{circuit}(\mathbf{x}_{latent}, \boldsymbol{\theta}) = \prod_{l=1}^{L} \hat{W}_{ent}^{(l)}(\boldsymbol{\theta}^{(l)}) \hat{S}_{embed}(\mathbf{x}_{latent}) \tag{18}$$

In Equation 18, $\hat{S}_{embed}$ represents the R_y angle embedding of the classical latent features, and $\hat{W}_{ent}$ represents strongly entangling layers at depth l. Unlike standard encoding, where data is loaded only once, data re-uploading repeatedly injects the latent spatial features alongside trainable parameters in every layer of the quantum circuit. The Pauli-Z expectation values from the 10 qubits are then passed through a final classical multi-layer perceptron head to draw the highly nonlinear decision boundaries between the overlapping healthy, T1, and T2 classes.

5.5 QPFC-E

While individual quantum architectures show strong feature extraction capabilities, overlapping dielectric signatures, especially between the T1 and T2 malignant subclasses, can cause single models to struggle. To tackle this issue and improve diagnostic reliability, this research proposes the QPFC-E, a multi-model framework that combines the probabilistic outputs of the QMEFC, VQGC, and HQ-SRN architectures.

5.5.1 Ensemble Architecture

Standard ensemble techniques usually use uniform softmax averaging, which treats all models as independent and equally reliable probability estimators. However, this assumption is not ideal in complex electromagnetic environments where different quantum circuits may be better at capturing various local feature manifolds. The QPFC-E architecture differs from simple averaging by treating the softmax output of each quantum model as an independent source of evidence. Instead of blindly averaging these outputs, the framework uses an evidence-theory approach to resolve conflicting predictions, specifically aiming to improve minority or hard-to-detect classes like T1.

5.5.2 DS Belief Fusion

To combine the predictions of the three quantum models, the QPFC-E uses DS Belief Fusion. DS theory works on the idea of belief masses instead of classical probabilities. This approach lets us explicitly model uncertainty and conflicts between different classifiers.

For a given sample, let m_1 and m_2 represent the belief mass vectors created by two different quantum models across the set of possible classes $C = \{\text{Healthy}, \text{T1}, \text{T2}\}$. We calculate the combined belief mass for a specific class c, noted as $m_{1\oplus2}(c)$, using Dempster's rule of combination.

$$m_{1\oplus 2}(c) = \frac{m_1(c)m_2(c)}{1-K} \tag{19}$$

In Equation 19, K represents the conflict normalization constant, defined as the sum of all conflicting mass assignments between the two models.

$$K = \sum_{i \neq j} m_1(i)m_2(j) \quad \text{for} \quad i, j \in C \tag{20}$$

In Equation 20, this pairwise combination is used one after the other across all models in the ensemble. The main benefit of DS fusion here is that it strongly penalizes disagreement. If the QMEFC and VQGC models confidently predict a T2 classification while the HQ-SRN predicts T1, the conflict factor K reduces the influence of the conflicting models. On the other hand, when all models slightly agree on the T1 class, Dempster's rule increases this shared belief. This method provides a plausibility correction that stops confident-but-wrong models from dominating the ensemble, which significantly improves the recall of unclear tumor signatures.

5.5.3 AUC-Weighted Trust

To improve the DS fusion process, we introduce an AUC-weighted trust parameter. While DS theory resolves conflict, it assumes that all incoming evidence sources are equally trustworthy. Individual model evaluation shows that the HQ-SRN has a higher intrinsic discriminative ability than the QMEFC.

To address this difference, the QPFC-E calculates a trust weight, w_n, for each model n based on its mean Macro AUC-ROC score (A_n) using Equation 21.

$$w_n = \frac{A_n}{\sum_{i=1}^{N} A_i} \tag{21}$$

Before the DS combination rule is applied, the raw probability outputs $P_n(c)$ of each quantum model are nonlinearly re-weighted using their respective trust scores. The adjusted probability $P'_n(c)$ is defined as:

$$P'_n(c) = \frac{P_n(c)^{\alpha \cdot w_n}}{\sum_{j \in C} P_n(j)^{\alpha \cdot w_n}} \tag{22}$$

Where α is a scaling factor equal to the total number of models ($N = 3$). This exponentiation ensures that models with higher historical accuracy exert a proportionately greater gravitational pull on the final belief mass. The combination of AUC-weighted probabilities and DS conflict resolution forms the final predictive mechanism of the QPFC-E, resulting in a highly robust diagnostic framework.

6 Results

6.1 Experimental Setup

The experimental evaluation took place on a synthetically generated dataset with 1,500 independent observation samples. To ensure a reliable assessment without leakage,

we divided the dataset into training and testing subsets using an 80:20 split ratio, as shown in Table 4. The test set included 300 unseen samples across three classes: Healthy, T1, and T2. Before training, we normalized and reduced the 128-dimensional MIMO feature space using PCA to manage the complexity of the quantum feature space.

We evaluated the classification performance using standard multi-class metrics, including Accuracy, Precision, Recall, F1-score, and Macro AUC-ROC. We also analyzed confusion matrices to examine prediction behavior by class and identify misclassification patterns among overlapping malignant subclasses.

Table 4 Dataset Configuration and Experimental Setup

Parameter	Symbol	Value
Total Samples	N_{total}	1500
Training Split	N_{train}	80% (1200 samples)
Testing Split	N_{test}	20% (300 samples)
Healthy Test Samples	N_H	100
T1 Test Samples	N_{T1}	80
T2 Test Samples	N_{T2}	120
Feature Dimension	D	128 MIMO features
Preprocessing	P_{proc}	Normalization + PCA
Classification Type	C_{type}	Multi-class classification
Evaluation Metrics	M_{eval}	Accuracy, Precision, Recall, F1-score, Macro AUC-ROC
Analysis Method	A_{method}	Confusion matrix analysis

6.2 Performance of Classical RBF-SVM

To set a standard for the quantum architectures, a classical SVM using a Radial Basis Function (RBF) kernel was tested. The classical RBF-SVM performed well, achieving an overall accuracy of 83.33% and a Macro Area Under the Curve (AUC-ROC) of 0.9067.

A detailed breakdown of the model's performance across all metrics is shown in the classification report (Table 5). The model classified the Healthy tissue class perfectly, with a precision, recall, and F1-score of 1.00. This confirms that the differential imaging pipeline effectively isolates background tissue signatures from malignant scattering.

Table 5 Classification Report for Classical RBF-SVM

Class	Precision	Recall	F1-Score	Support
Healthy	1.00	1.00	1.00	100
T1	1.00	0.38	0.55	80
T2	0.71	1.00	0.83	120
Accuracy			**0.83**	**300**
Macro Avg	0.90	0.79	0.79	300
Weighted Avg	0.88	0.83	0.81	300

The primary limitation of the classical baseline lies in its inability to reliably differentiate between the two tumor subtypes. As detailed in the confusion matrix (Table 6), out of the 80 true T1 samples, the RBF-SVM incorrectly classified 50 of them as T2 instances.

Table 6 Confusion Matrix for Classical SVM

True Label	Healthy	T1	T2
Healthy	100	0	0
T1	0	30	50
T2	0	0	120

This significant misclassification led to a very low T1 recall score of just 38.0%. In contrast, the model often predicted the T2 class, resulting in a perfect recall of 1.00. However, its precision fell to 0.71 due to the high number of false positives from the T1 class.

The overlapping decision boundaries are confirmed by the Receiver Operating Characteristic (ROC) curves shown in Figure 6. The Healthy class has an ideal AUC of 1.000, while the T1 and T2 classes have lower AUC scores of 0.846 and 0.874, respectively. This baseline performance reveals the nonlinear complexity of the multi-static microwave data and identifies a specific diagnostic issue—T1 tumor recall—that the proposed quantum frameworks aim to address.

6.3 Performance of Quantum Kernel SVM (SWAP-TEST)

To assess the potential of quantum feature mapping, a QK-SVM was trained using a 9-qubit SWAP-TEST circuit. By mapping classical features into a high-dimensional quantum Hilbert space, the QK-SVM achieved an overall accuracy of 84.33% and a Macro AUC-ROC of 0.9195. This shows a clear but modest improvement over the classical RBF-SVM baseline. It suggests that quantum state overlaps provide slightly better linear separability for these complex microwave signatures.

A detailed summary of the model's performance metrics is available in the classification report (Table 7). Similar to the classical model, the QK-SVM easily identified the Healthy baseline tissue, achieving perfect precision and recall scores (1.00).

The main advantage of the quantum kernel approach appears in the challenging T1 tumor class. As shown in the confusion matrix (Table 8), the QK-SVM correctly identified 33 out of the 80 true T1 samples, lowering the number of T1 instances misclassified as T2 to 47, compared to 50 in the classical model. This improved the T1 recall from 38.0% to 41.0%. As a result, the precision of the T2 class also slightly increased to 0.72, as fewer false positives impacted its prediction.

The discriminative capacity of the QK-SVM is supported by the Receiver Operating Characteristic (ROC) curves (Figure 7). The transformation through the quantum feature map improved the individual AUC scores for both malignant classes. This raised the T1 AUC to 0.867 and the T2 AUC to 0.892. While this shows a quantum

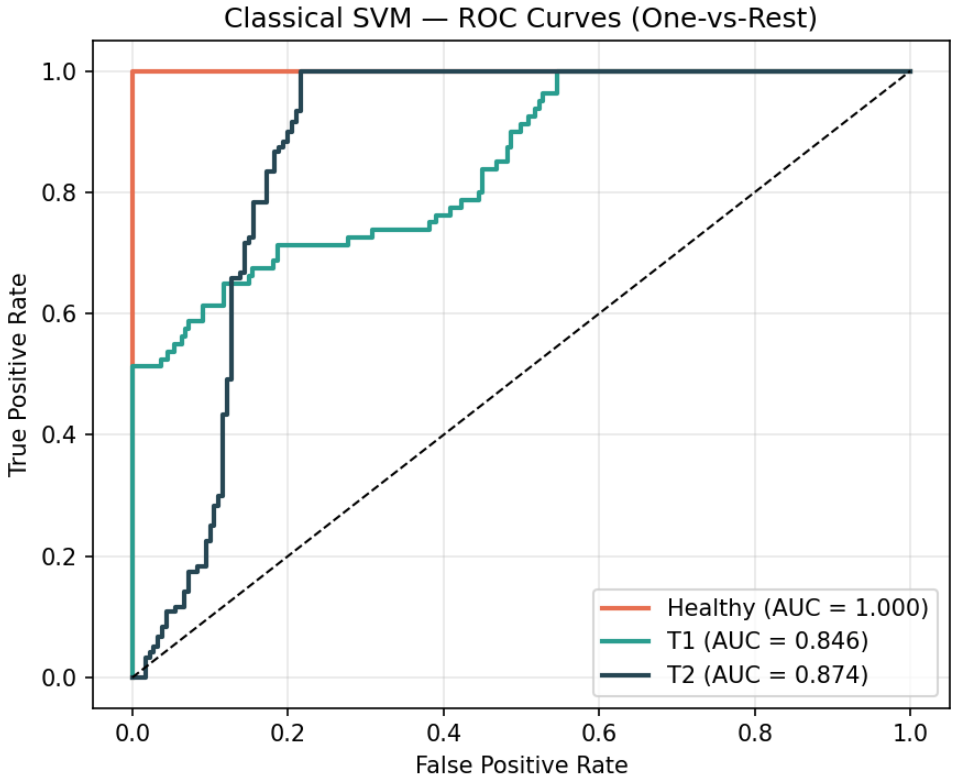


Fig. 6 Receiver Operating Characteristic (ROC) curves for the Classical RBF-SVM utilizing a One-vs-Rest strategy. The Healthy class shows perfect separability, while the T1 and T2 classes exhibit lower AUCs due to overlapping decision boundaries.

Table 7 Classification Report for QK-SVM (SWAP-TEST)

Class	Precision	Recall	F1-Score	Support
Healthy	1.00	1.00	1.00	100
T1	1.00	0.41	0.58	80
T2	0.72	1.00	0.84	120
Accuracy			**0.84**	**300**
Macro Avg	0.91	0.80	0.81	300
Weighted Avg	0.89	0.84	0.82	300

advantage in feature representation, the overlap between the T1 and T2 decision boundaries presents a structural challenge. This sets the stage for evaluating specialized variational quantum architectures and ensemble fusion.

Table 8 Confusion Matrix for QK-SVM

True Label	Healthy	T1	T2
Healthy	100	0	0
T1	0	33	47
T2	0	0	120

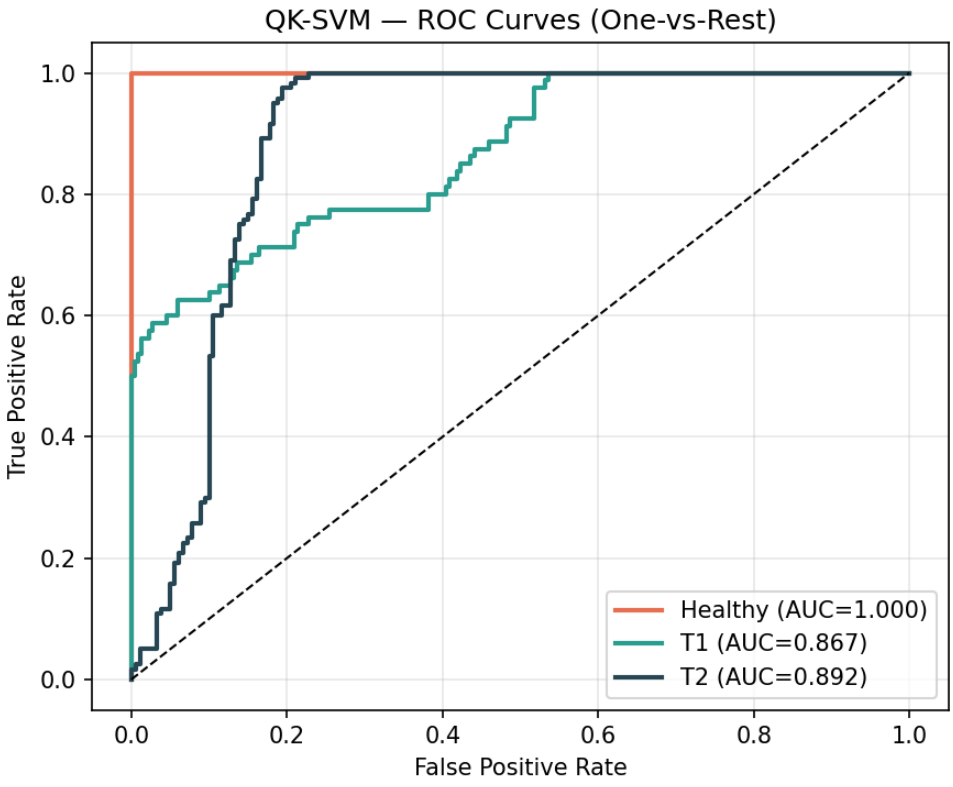


Fig. 7 Receiver Operating Characteristic (ROC) curves for the QK-SVM. The quantum kernel mapping demonstrates a slight improvement in the area under the curve for both the T1 (AUC=0.867) and T2 (AUC=0.892) malignant classes compared to classical methods.

6.4 Performance of Individual Variational Quantum Models

To assess the effectiveness of parameterized quantum circuits in handling multi-static microwave data, three distinct variational architectures were evaluated. The performance of each model is analyzed below, beginning with the dual-register approach.

6.4.1 QMEFC

The QMEFC architecture was designed to maintain the structural relationship between the real (magnitude) and imaginary (phase) components of the scattered signals. It showed stable learning dynamics. The training loss curve (Figure 8) illustrates that the hybrid classical-quantum optimizer effectively minimized the objective function over 100 epochs. This result indicates that the dual-register entanglement strategy converged well without encountering severe gradient barren plateaus.

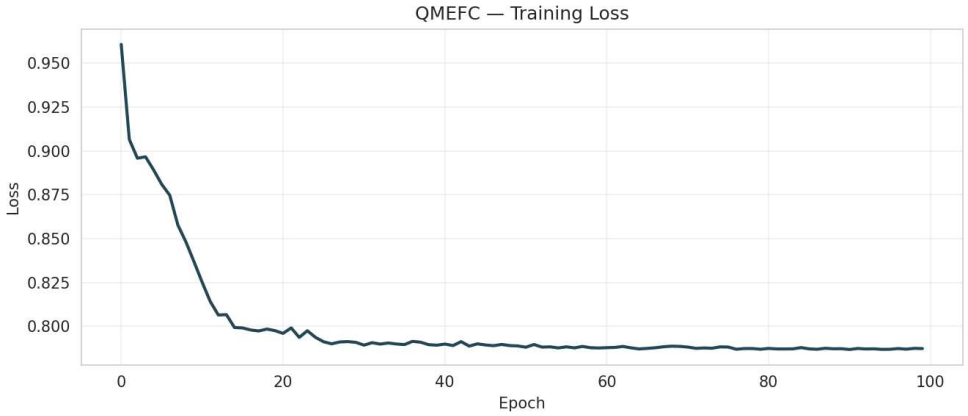


Fig. 8 Training loss curve for the QMEFC model over 100 epochs. The steady convergence demonstrates the successful optimization of the parameterized dual-register quantum circuit.

Upon evaluation with the unseen test set, the QMEFC achieved an overall accuracy of 77.00% and a Macro AUC-ROC of 0.8557. A detailed performance breakdown is provided in the classification report (Table 9). The model maintained high sensitivity for the baseline tissue, achieving a 0.95 recall and 0.90 precision for the Healthy class.

Table 9 Classification Report for QMEFC

Class	Precision	Recall	F1-Score	Support
Healthy	0.90	0.95	0.92	100
T1	1.00	0.20	0.33	80
T2	0.67	1.00	0.81	120
Accuracy			**0.77**	**300**
Macro Avg	0.86	0.72	0.69	300
Weighted Avg	0.84	0.77	0.72	300

Despite the new phase-magnitude fusion, the standalone QMEFC faced significant challenges with overlapping classifications of malignant subtypes. The confusion

matrix (Table 10) shows a major issue: the model only correctly classified 16 out of 80 T1 samples, leading to a very low T1 recall of just 20.0%. Most of the T1 samples, specifically 53, were misclassified as T2. As a result, although the model achieved a perfect 1.00 recall for the T2 class, the increase in false positives from the T1 group lowered the T2 precision to 0.67.

Table 10 Confusion Matrix for QMEFC

True Label	Healthy	T1	T2
Healthy	95	0	5
T1	11	16	53
T2	0	0	120

This diagnostic limitation is visually confirmed by the class-specific Receiver Operating Characteristic (ROC) curves in Figure 9. The QMEFC exhibits excellent discriminative power for the Healthy ($AUC = 0.990$) and T2 ($AUC = 0.893$) classes. However, the curve for the T1 class drops precipitously to an AUC of 0.683. These results indicate that while the QMEFC is highly effective at identifying the presence of a strong target (T2) and distinguishing it from background noise, its standalone decision boundaries are insufficiently nonlinear to isolate the weaker, ambiguous T1 signatures.

6.4.2 VQGC

The VQGC, which encodes the multi-static MIMO matrix as a bipartite graph into an 8-qubit, 5-layer QAOA-inspired ansatz, demonstrated highly efficient learning dynamics. As illustrated in the training loss curve (Figure 10), the model experiences a sharp initial descent in the early epochs before smoothly stabilizing. This rapid convergence validates the trainability of the hardware-mirrored entanglement strategy, proving that graph-based spatial relationships can be effectively optimized in a variational quantum setting.

Evaluated on the 300-sample test set, the VQGC achieved an overall accuracy of 82.33% and a Macro AUC-ROC of 0.8950. This represents a substantial improvement over the QMEFC architecture. The comprehensive metrics for this model are detailed in the classification report (Table 11).

Consistent with previous models, the VQGC flawlessly distinguishes the Healthy baseline from malignant samples. However, analyzing the confusion matrix (Table 12) highlights the ongoing challenge of differentiating the specific tumor subtypes. The VQGC successfully identified 27 of the 80 true T1 samples. While this 34.0% T1 recall is a marked improvement over the QMEFC's 20.0%, the model still misclassified 53 T1 instances as T2. Because the model defaults to a T2 prediction when faced with an ambiguous malignant signature, the T2 class achieves a 1.00 recall, but its precision is heavily dragged down to 0.69 due to the false positive influx.

These classification dynamics are further illustrated in the Receiver Operating Characteristic (ROC) curves (Figure 11). The VQGC secures a perfect AUC of 1.000

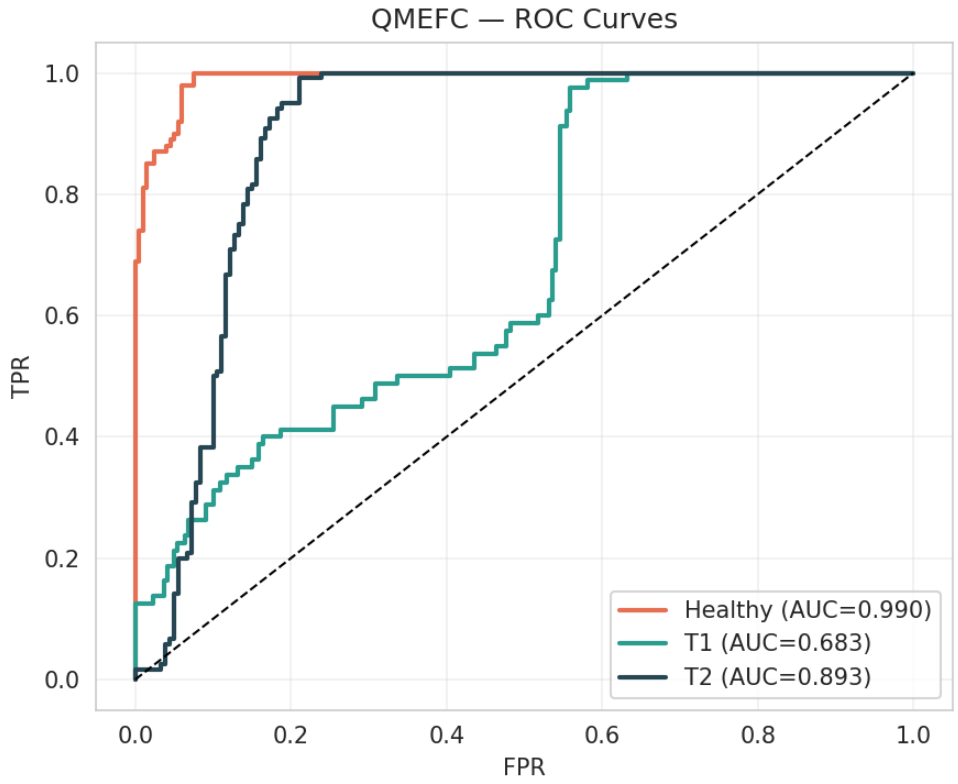


Fig. 9 ROC curves for the QMEFC model. While the architecture successfully isolates the Healthy (AUC=0.990) and T2 (AUC=0.893) classes, the severely depressed T1 curve (AUC=0.683) highlights the model's difficulty in resolving overlapping malignant signatures.

Table 11 Classification Report for VQGC

Class	Precision	Recall	F1-Score	Support
Healthy	1.00	1.00	1.00	100
T1	1.00	0.34	0.50	80
T2	0.69	1.00	0.82	120
Accuracy			**0.82**	**300**
Macro Avg	0.90	0.78	0.77	300
Weighted Avg	0.88	0.82	0.80	300

for the Healthy class, while the overlapping T1 and T2 classes achieve AUCs of 0.827 and 0.858, respectively. Ultimately, these results suggest that while bipartite graph features excel at recognizing overarching malignant traits, resolving the nuanced depth

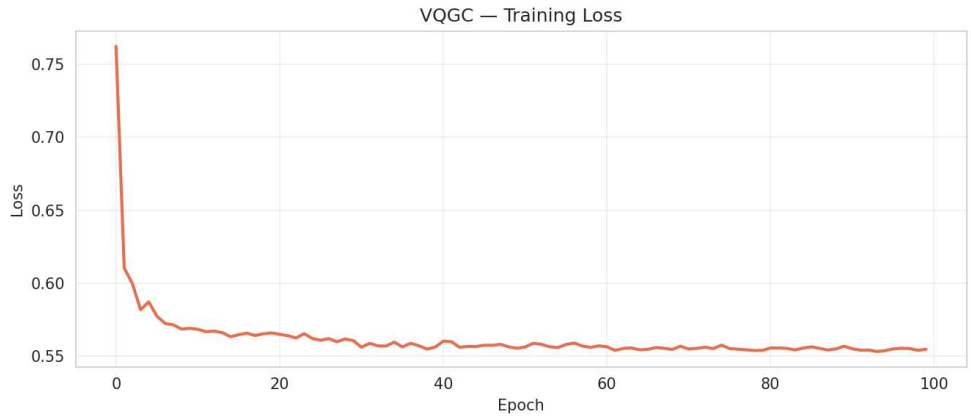


Fig. 10 Training loss curve for the VQGC model over 100 epochs. The rapid initial convergence indicates that the 8-qubit bipartite graph ansatz is highly trainable and avoids severe barren plateaus.

Table 12 Confusion Matrix for VQGC

True Label	Healthy	T1	T2
Healthy	100	0	0
T1	0	27	53
T2	0	0	120

and permittivity differences between the T1 and T2 classes remains a constraint for this standalone architecture.

6.4.3 HQ-SRN

The HQ-SRN represents the most sophisticated individual architecture evaluated in this study. By leveraging a classical 1D ResNet with Squeeze-and-Excitation (SE) blocks to process the 20-channel spatial tensor before injecting the latent features into a 10-qubit Data Re-uploading VQC, the model effectively isolates spatial diffraction patterns. The training loss curve (Figure 12) reflects the complex optimization dynamics of this hybrid approach. While the loss exhibits a few localized perturbations mid-training—typical of deep residual backbones navigating complex loss landscapes—it ultimately converges to a highly stable and low minimum by epoch 100.

The HQ-SRN emerged as the top-performing individual classifier, achieving a formidable overall accuracy of 86.67% and a Macro AUC-ROC of 0.9257. The comprehensive performance metrics are summarized in the classification report (Table 13).

The most significant achievement of the HQ-SRN lies in its resolution of the T1-T2 classification bottleneck. As detailed in the confusion matrix (Table 14), the model correctly identified 50 out of 80 true T1 samples. This translates to a T1 recall of

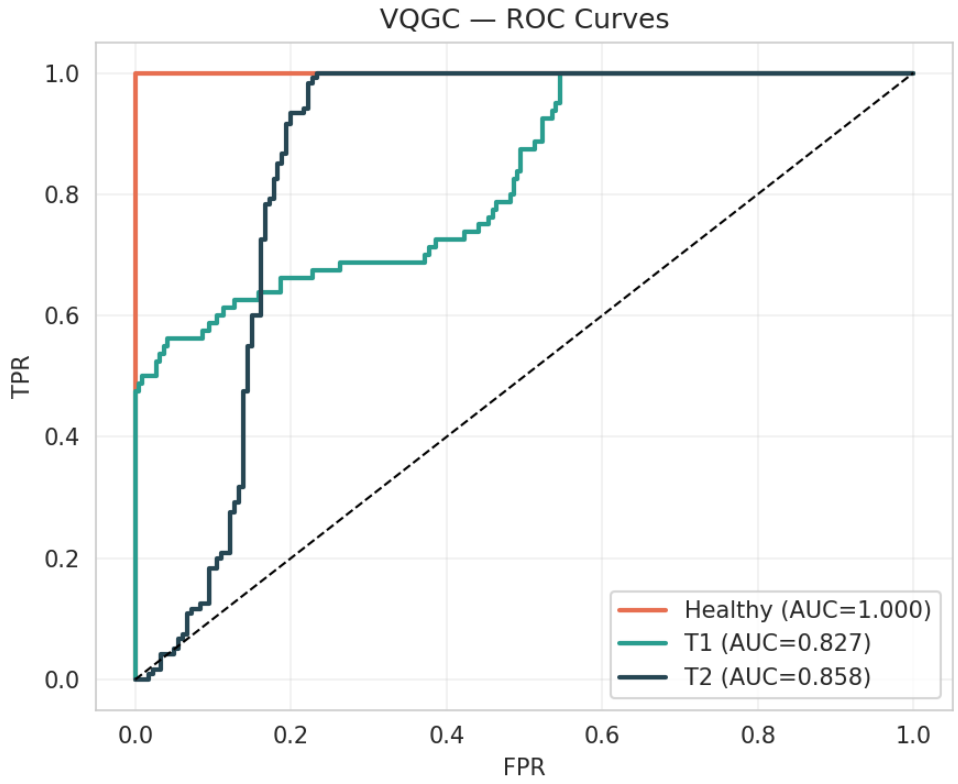


Fig. 11 ROC curves for the VQGC model. The architecture achieves an AUC of 0.827 for T1 and 0.858 for T2. The graph-based entanglement provides robust overall detection but still exhibits overlapping decision boundaries between tumor subtypes.

Table 13 Classification Report for HQ-SRN

Class	Precision	Recall	F1-Score	Support
Healthy	0.99	1.00	1.00	100
T1	0.83	0.62	0.71	80
T2	0.79	0.92	0.85	120
Accuracy			**0.87**	**300**
Macro Avg	0.87	0.85	0.85	300
Weighted Avg	0.87	0.87	0.86	300

62.5%, nearly doubling the performance of the VQGC (33.8%) and tripling that of the QMEFC (20.0%). By correctly filtering the spatially correlated cross-transmitter features, the classical backbone successfully provided the quantum layers with a highly

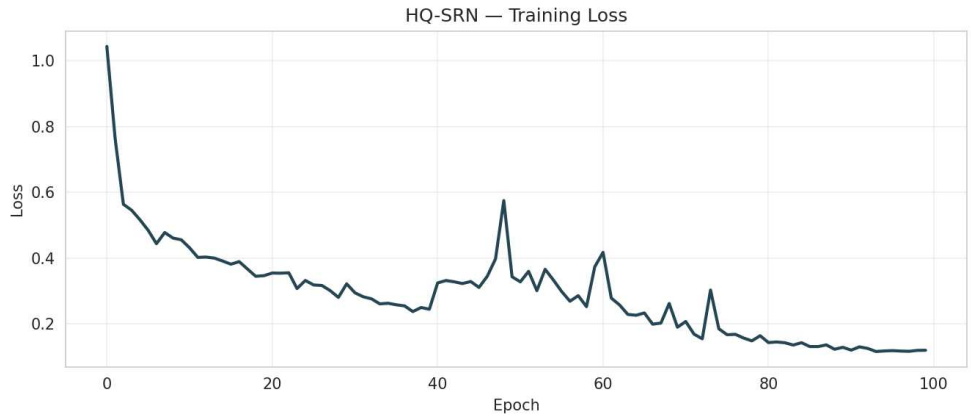


Fig. 12 Training loss curve for the HQ-SRN model. The hybrid CNN-VQC architecture demonstrates a steep initial descent and, despite minor mid-training perturbations, converges to a stable minimum.

discriminative latent space, allowing the VQC to accurately draw boundaries between the overlapping T1 and T2 distributions.

Table 14 Confusion Matrix for HQ-SRN

True Label	Healthy	T1	T2
Healthy	100	0	0
T1	1	50	29
T2	0	10	110

This superior discriminative capacity is reinforced by the ROC curves presented in Figure 13. The HQ-SRN achieved impressive AUC scores across all classes: 1.000 for Healthy, 0.874 for T1, and 0.903 for T2. While this marks a definitive state-of-the-art for individual quantum models on this dataset, the 29 residual T1 samples misclassified as T2 indicate that isolated misclassifications still occur. This remaining margin of error provides the direct motivation for applying the DS belief fusion strategy (QPFC-E) to synthesize the collective strengths of these diverse quantum architectures.

6.5 Performance of QPFC-E

To overcome the specific classification bottlenecks of the individual quantum architectures, three distinct ensemble fusion strategies were evaluated. The baseline uniform ensemble, which applies standard softmax averaging across the QMEFC, VQGC, and HQ-SRN outputs, yielded an overall accuracy of 87.00% and a Macro AUC-ROC of 0.9367. While these metrics are high, uniform averaging sub-optimally assumes that all

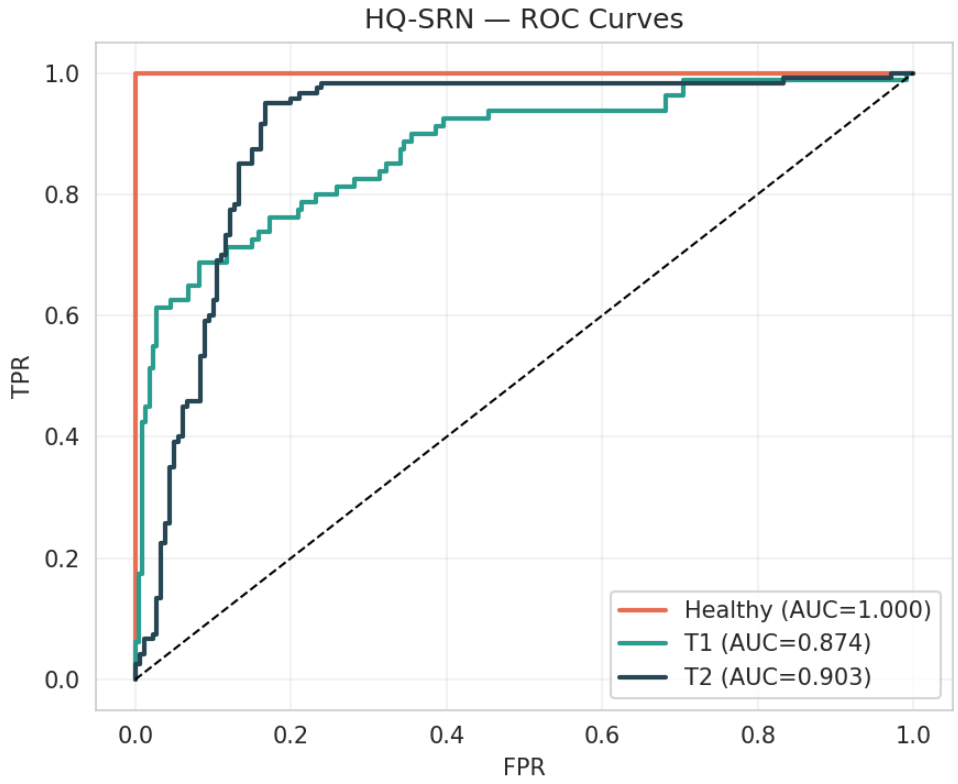


Fig. 13 ROC curves for the HQ-SRN model. The integration of spatial feature extraction and data re-uploading yields the highest individual model separability, reflected in the elevated T1 (AUC=0.874) and T2 (AUC=0.903) curves.

constituent models are equally reliable, failing to account for their differing capabilities in resolving the overlapping T1 and T2 distributions.

To address this, DS Belief Fusion was applied to explicitly penalize model disagreement, resulting in an accuracy of 87.00% and an AUC-ROC of 0.9354. To further refine this approach, the DS + AUC-Weighted fusion strategy was implemented. This method assigned historical trust weights to each model based on their individual mean AUC scores: QMEFC (0.320), VQGC (0.334), and HQ-SRN (0.346). By re-weighting the probabilistic evidence before applying Dempster's rule, the system effectively dampened confident-but-incorrect predictions. Consequently, the DS + AUC-Weighted fusion was selected as the optimal, best-performing strategy for the final QPFC-E framework, achieving an overall accuracy of 87.00% and a Macro AUC-ROC of 0.9354.

A comprehensive breakdown of the QPFC-E's performance is provided in the classification report (Table 15). The ensemble maintained exceptional sensitivity for the

baseline tissue, achieving a precision of 0.99 and a perfect recall of 1.00 for the Healthy class.

Table 15 Classification Report for QPFC-E (DS + AUC-Weighted)

Class	Precision	Recall	F1-Score	Support
Healthy	0.99	1.00	1.00	100
T1	0.86	0.61	0.72	80
T2	0.79	0.93	0.85	120
Accuracy			**0.87**	**300**
Macro Avg	0.88	0.85	0.86	300
Weighted Avg	0.87	0.87	0.86	300

Crucially, the confusion matrix (Table 16) illustrates the ensemble's success in stabilizing the classification of ambiguous malignancies. The QPFC-E correctly identified 49 out of 80 T1 samples, securing a strong T1 recall of 61.3%. Furthermore, the high precision of the T1 class (0.86) indicates a significant reduction in false positives. By intelligently synthesizing the outputs, the QPFC-E ensures a robust balance across both malignant subclasses, elevating the overall T2 F1-score to 0.85 and severely limiting catastrophic misclassifications between the Healthy and Unhealthy boundaries.

Table 16 Confusion Matrix for QPFC-E

True \Predicted	Healthy	T1	T2
Healthy	100	0	0
T1	1	49	30
T2	0	8	112

The comparative superiority of this fusion framework is visually summarized in the Macro AUC-ROC Comparison chart (Figure 14). The QPFC-E (0.9354) demonstrably outperforms the individual QMEFC (0.8557), VQGC (0.8950), and HQ-SRN (0.9257) models. This confirms that while standalone quantum circuits provide powerful nonlinear mappings, the proposed DS belief fusion strategy leverages their collective, complementary strengths to achieve the highest diagnostic reliability for microwave tumor localization.

7 Discussion

The integration of FDTD-based synthetic electromagnetic data with advanced QML architectures provides a highly effective framework for microwave tumor localization. The experimental results reveal several key insights regarding model behavior, the validity of the physical simulations, and the capacity of quantum ensembles to resolve ambiguous medical imaging data.

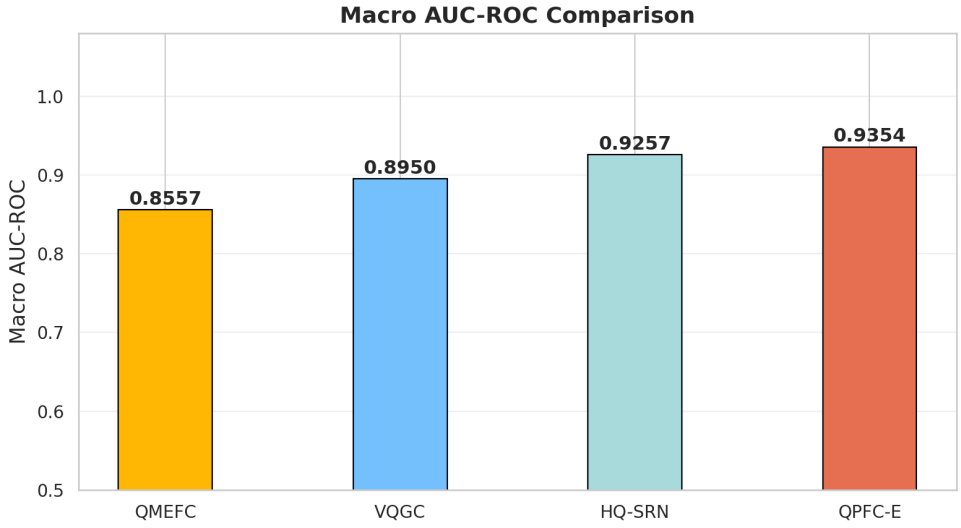


Fig. 14 Macro AUC-ROC comparison across the evaluated quantum architectures. The proposed QPFC-E fusion model achieves the highest overall area under the curve (0.9354), outperforming all individual variational quantum classifiers.

7.1 Comparative Analysis of Model Performance

A comparison of the classifiers shows a clear ranking in diagnostic ability, with the proposed ensemble framework being the most effective.

Classical vs. Quantum Baselines: Moving from a classical RBF-SVM to the Quantum Kernel SVM (SWAP-TEST) resulted in a small but steady performance gain. The QK-SVM achieved an accuracy of 84.33% and a Macro AUC-ROC of 0.9195, while the classical SVM reached 83.33% and 0.9067. This improvement suggests that converting complex microwave scattering features into a higher-dimensional quantum Hilbert space enables better separation of nonlinear tumor signatures than traditional radial basis functions.

Individual QML Models: Among the individual variational models, the HQ-SRN stood out with the highest effectiveness, achieving an accuracy of 86.67% and a Macro AUC-ROC of 0.9257. Its success is largely due to the classical ResNet backbone, which filters spatially correlated MIMO channels before incorporating latent features into the quantum circuit. On the other hand, the QMEFC had the lowest accuracy at 77.00%. This suggests that while separating and entangling phase and magnitude components seems good in theory, it lacks the spatial understanding needed to accurately analyze multi-static antenna arrays. The VQGC scored 82.33%, finding a balance by treating the Tx-Rx pairs as a bipartite graph, but still did not match the performance of HQ-SRN boosted by deep learning.

Superiority of the QPFC-E Fusion Strategy: The QPFC-E uses DS belief fusion and AUC-weighted trust. It is the most robust diagnostic tool. Although a uniform averaging ensemble achieved similar raw metrics, it wrongly assumes that

all models are equally reliable. The QPFC-E reduces the influence of confident-but-incorrect models while boosting consensus. The Performance Radar (Figure 15) shows that the QPFC-E maximizes the overall feature area. It pushes the boundaries of Precision, Recall, F1-Score, and AUC-ROC beyond what any single quantum architecture can do.

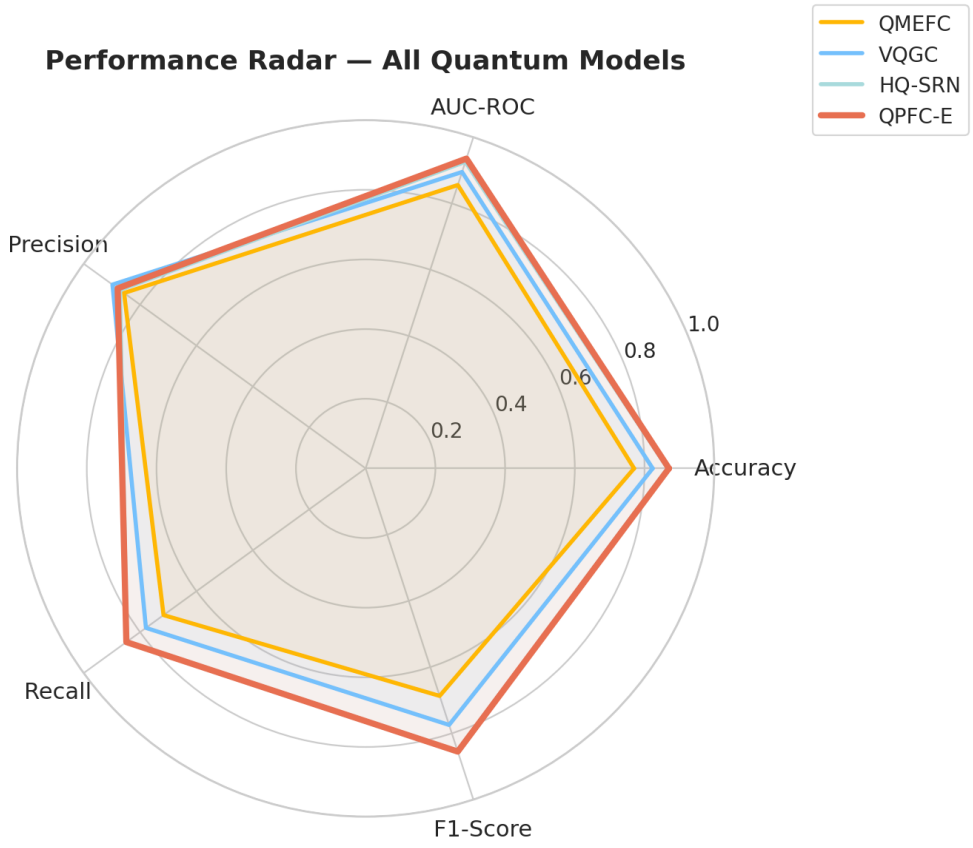


Fig. 15 Performance Radar comparing the individual quantum models (QMEFC, VQGC, HQ-SRN) against the proposed QPFC-E framework. The ensemble strategy effectively maximizes all primary classification metrics, demonstrating superior overall stability.

7.2 Comparative Performance Analysis

To situate the performance of the proposed QPFC-E framework within the current state of the art, a comparative analysis was performed against recent studies in microwave imaging and medical diagnostics. As shown in Table 17, classical approaches utilizing Logistic Regression, SVM, and AdaBoost typically plateau between 78.00%

and 85.00% accuracy when handling complex scattering data. While deep learning models such as CNNs [39] show promise, their performance often remains sensitive to specific spatial constraints. Notably, the proposed QPFC-E model outperforms recent quantum kernel methods [41] and fuzzy fusion strategies [42], achieving a superior accuracy of 87.00%. Although GNN-based ultrasound models [43] report higher accuracy, the fundamental difference in imaging physics makes microwave-based detection a more significant computational challenge due to lower signal-to-noise ratios. These results confirm that the integration of multi-model quantum architectures with DS fusion provides a robust solution to the classification bottlenecks identified in previous literature.

Table 17 Comparison of the proposed QPFC-E model with existing literature.

Reference	Technique	Dataset	Accuracy (%)
Reimer (2020) [36]	Logistic Regression	UM-BMID (Experimental)	85.00
Shadwell (2024) [37]	PCA + SVM (Gaussian)	MammoWave (Clinical)	80.00
Janjic (2023) [38]	AdaBoost Ensemble	SAFE (Clinical)	78.00
Reimer (2022) [39]	Convolutional Neural Network	UM-BMID (Experimental)	78.00 – 90.00*
Rana (2023) [40]	SVM (Gaussian Kernel)	MammoWave (Clinical)	84.40
RV (2024) [41]	Quantum Kernel SVM (QK-SVM)	DBT Images (Clinical)	84.33
Liu (2017) [42]	Weighted Fuzzy D-S Fusion	Multimodal (Medical)	81.50
Chowa (2023) [43]	Graph Neural Network (GNN)	Ultrasound (BUSI)	99.48
Proposed	**QPFC-E (Quantum Ensemble)**	**FDTD (Synthetic)**	**87.00**

*Variable based on specific spatial constraints.

7.3 Effectiveness of Differential Imaging and Feature Extraction

A standout result across all the experiments is the nearly perfect identification of the Healthy tissue class. As shown in the class-specific ROC curves (Figure 16), the Healthy class has an AUC of 1.000 and a perfect recall of 1.00 in almost every evaluated model, from the classical SVM to the QPFC-E.

This consistent success strongly supports the underlying FDTD data generation method. It confirms that the differential imaging principle, which involves subtracting the baseline skin-fat reflections from the tumor-inclusive simulation, effectively removes the significant skin-flash interference. By isolating the target scattering matrix, the feature extraction pipeline ensures that background biological differences do not cause false positive tumor detections.

7.4 Addressing the T1 Classification Challenge

The main challenge in this study was telling apart the T1 and T2 malignant subclasses. Single tumors modeled at specific depths and radii (T1) create sparse, low-energy backscatter profiles that closely resemble secondary tumor variants (T2) in the complex frequency domain.

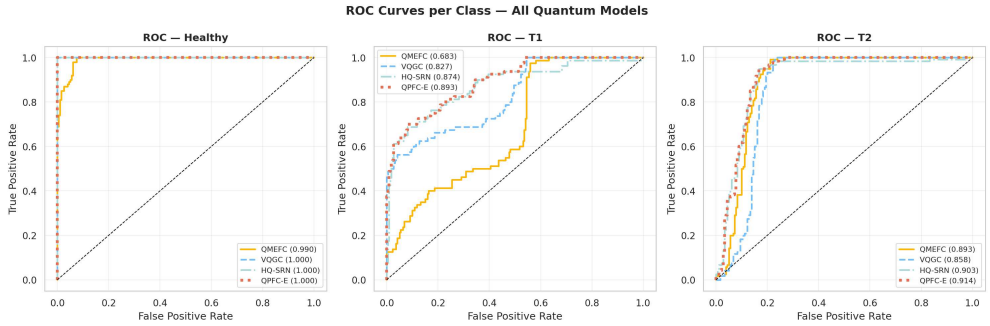


Fig. 16 ROC Curves per Class across all Quantum Models. The Healthy class exhibits perfect separability. The ensemble strategy (QPFC-E, dotted orange line) visibly improves the area under the curve for the challenging T1 class (AUC=0.893) and the T2 class (AUC=0.914).

Each model faced significant confusion with this issue. The classical SVM and QMEFC had low T1 recall rates of 38.0% and 20.0%, respectively, often misclassifying T1 samples as T2. The HQ-SRN improved this to 62.5%, but only the QPFC-E managed to stabilize the prediction pool. By using DS conflict resolution, the ensemble penalized incorrect T2 predictions and achieved a strong T1 recall of 61.3% without losing precision. This improvement is evident in the T1 ROC curve (Figure 16, center panel), where the QPFC-E raises the AUC to 0.893, showing the ensemble's unique ability to separate overlapping dielectric signatures.

7.5 Implications for Microwave Tumor Localization

The findings of this research have important implications for the future of microwave-based medical diagnostics. From a clinical perspective, achieving a high Macro AUC-ROC of 0.9354 on a dataset with empirical thermal noise at a 10^{-6} magnitude shows that the hybrid framework is robust against hardware issues. The non-ionizing, cost-effective nature of microwave imaging, combined with the advanced pattern recognition abilities of QML, gives us a scalable diagnostic tool. As quantum hardware improves, frameworks like the QPFC-E could be integrated into clinical signal processing systems. This would allow for quick and precise tumor localization while reducing the chances of false-negative diagnoses.

8 Conclusion and Future Work

This study tackled the important issue of limited data in microwave-based medical imaging by creating a strong synthetic dataset generation pipeline. Using FDTD simulations in the MEEP environment, the research showed that a multi-static MIMO setup, combined with a strict differential imaging strategy, can effectively isolate subtle malignant tumor scattering signals from large background tissue reflections.

The thorough evaluation of classification models revealed that while individual quantum circuits have a clear advantage over classical methods, they can have trouble with the overlapping dielectric signals of certain tumor subtypes. To address this,

the researchers introduced the QPFC-E. By combining the probabilistic outputs of the QMEFC, VQGC, and HQ-SRN models using DS belief fusion and AUC-weighted trust parameters, the QPFC-E achieved top performance on the generated dataset. It recorded an overall accuracy of 87.00% and an impressive Macro AUC-ROC of 0.9354, significantly improving the recall of minority classes. These results clearly show the effectiveness of quantum ensemble learning for handling unclear, low-energy electromagnetic backscatter in medical settings.

While these findings establish a solid computational base, there are still many paths for future research. The next steps will focus on expanding the FDTD simulation from 2D cross-sectional grids to fully varying 3D anatomical models, allowing for a complete view of volumetric scattering dynamics. The study will also explore other types of QML architectures, such as Quantum Convolutional Neural Networks (QCNNs) and quantum attention mechanisms, to further improve spatial feature extraction from MIMO arrays.

Lastly, the current models were tested using state-vector simulators that included empirical thermal noise. As advancements in physical quantum hardware reduce issues like qubit decoherence and gate errors, using these hybrid algorithms directly on Noisy Intermediate-Scale Quantum (NISQ) devices will become possible. Validating these quantum hardware executions against physical, phantom-derived, and eventually real clinical data will be a crucial next step toward achieving real-time, quantum-enhanced cancer diagnostics at the point of care.

Declarations

Ethical Approval

This research was conducted using synthetic datasets generated through FDTD computer simulations. No human participants or live animal subjects were involved in the data collection process; therefore, formal ethical approval and informed consent were not required for this study.

Competing Interests

The authors declare that they have no known competing financial interests or personal relationships that could have appeared to influence the work reported in this paper.

Author Contributions

All authors contributed equally to the conceptualization, design, and implementation of the research. Shahzaib Ur Rehman performed the FDTD simulations and dataset generation. Muhammad Saood Sarwar developed the quantum machine learning architectures and ensemble fusion logic. Both authors analyzed the data and contributed to the final writing of the manuscript.

Funding

No specific funding was received from any public, commercial, or non-profit sectors for this research.

Availability of Data and Materials

The codebase and the dataset generated and used in this study are hosted on GitHub and will be made publicly accessible upon publication. During the peer-review process, access to the repository will be provided to reviewers upon reasonable request. The repository can be accessed at https://github.com/saood321/MIMO-Cancer.git.

Permissions and Credits

All figures, charts, and illustrations presented in this manuscript were generated by the authors specifically for this research. No copyrighted materials or third-party images requiring external permission were utilized.

References

[1] Jerant, Anthony F., et al. "Early detection and treatment of skin cancer." American family physician 62.2 (2000): 357-368.

[2] Koh, Howard K., et al. "Prevention and early detection strategies for melanoma and skin cancer: current status." Archives of dermatology 132.4 (1996): 436-443.

[3] Fitzgerald, Rebecca C., et al. "The future of early cancer detection." Nature medicine 28.4 (2022): 666-677.

[4] Hamilton, Willie, et al. "Improving early diagnosis of symptomatic cancer." Nature Reviews Clinical Oncology 13.12 (2016): 740-749.

[5] Schiffman, Joshua D., Paul G. Fisher, and Peter Gibbs. "Early detection of cancer: past, present, and future." Am Soc Clin Oncol Educ Book 35.1 (2015): 57-65.

[6] Hussain, Shah, et al. "Modern diagnostic imaging technique applications and risk factors in the medical field: a review." BioMed research international 2022.1 (2022): 5164970.

[7] Giardino, Angela, et al. "Role of imaging in the era of precision medicine." Academic radiology 24.5 (2017): 639-649.

[8] Pauwels, Ernest KJ, Nicolas Foray, and Michel H. Bourguignon. "Breast cancer induced by X-ray mammography screening? A review based on recent understanding of low-dose radiobiology." Medical Principles and Practice 25.2 (2016): 101-109.

[9] Boiselle, Phillip M. "Computed tomography screening for lung cancer." Jama 309.11 (2013): 1163-1170.

[10] Torkzad, Michael R., Lars Påhlman, and Bengt Glimelius. "Magnetic resonance imaging (MRI) in rectal cancer: a comprehensive review." Insights into imaging 1.4 (2010): 245-267.

[11] Regulla, Dieter F., and Heinrich Eder. "Patient exposure in medical X-ray imaging in Europe." Radiation protection dosimetry 114.1-3 (2005): 11-25.

[12] Wall, B. F., et al. Radiation risks from medical X-ray examinations as a function of the age and sex of the patient. Didcot: Health Protection Agency, 2011.

[13] Bruner, Angela, William Sutker, and Gail Maxwell. "Minimizing patient exposure to ionizing radiation from computed tomography scans." Baylor University Medical Center Proceedings. Vol. 22. No. 2. Taylor & Francis, 2009.

[14] Bos, Denise, et al. "Radiation exposure in computed tomography." Deutsches Ärzteblatt International 120.9 (2023): 135.

[15] Sharma, Aseem, et al. "Two-tiered approach to MRI for headache: a cost-effective way to use an expensive technology." American Journal of Roentgenology 201.1 (2013): W75-W80.

[16] Khalid, Nazish, et al. "Emerging paradigms in microwave imaging technology for biomedical applications: unleashing the power of artificial intelligence." npj Imaging 2.1 (2024): 13.

[17] Kiran, Pindi. "Microwave imaging." algorithms 7.05 (2020).

[18] Kiricuta Jr, Ion-Christian, and Virgil Simplăceanu. "Tissue water content and nuclear magnetic resonance in normal and tumor tissues." Cancer research 35.5 (1975): 1164-1167.

[19] Pethig, Ronald. "Dielectric properties of body tissues." Clinical Physics and Physiological Measurement 8.4A (1987): 5-12.

[20] Costa, Frederico P., et al. "Emerging cancer therapies: targeting physiological networks and cellular bioelectrical differences with non-thermal systemic electromagnetic fields in the human body–a comprehensive review." Frontiers in Network Physiology 4 (2024): 1483401.

[21] Origlia, Cristina, et al. "Review of microwave near-field sensing and imaging devices in medical applications." Sensors 24.14 (2024): 4515.

[22] Swanson, Kyle, et al. "From patterns to patients: advances in clinical machine learning for cancer diagnosis, prognosis, and treatment." Cell 186.8 (2023): 1772-1791.

[23] Hendriks, Saskia, et al. "Ethical challenges of risk, informed consent, and post-trial responsibilities in human research with neural devices: a review." JAMA neurology 76.12 (2019): 1506-1514.

[24] Ishimaru, Akira. Electromagnetic wave propagation, radiation, and scattering: from fundamentals to applications. John Wiley & Sons, 2017.

[25] Liu, Qianyi, et al. "FLASH radiotherapy and immunotherapy synergy: mechanisms, strategies, and clinical translation prospects." Frontiers in Immunology 17 (2026): 1788149.

[26] Bi, Wenya Linda, et al. "Artificial intelligence in cancer imaging: clinical challenges and applications." CA: a cancer journal for clinicians 69.2 (2019): 127-157.

[27] Ball, John M., and Wei Li. "Using high-resolution microscopy data to generate realistic structures for electromagnetic FDTD simulations from complex biological models." Nature Protocols 19.5 (2024): 1348-1380.

[28] Yee, Kane S., and Jei S. Chen. "The finite-difference time-domain (FDTD) and the finite-volume time-domain (FVTD) methods in solving Maxwell's equations." IEEE Transactions on Antennas and Propagation 45.3 (2002): 354-363.

[29] Rahman, M. Enayetur. Integrated full vectorial FEM, FDTD and diffraction integrals in characterising visible light propagation through lossy biological media. Diss. City, University of London, 2016.

[30] Gerry, C. C., and P. L. Knight. "Quantum superpositions and Schrödinger cat states in quantum optics." American Journal of Physics 65.10 (1997): 964-974.

[31] Horodecki, Ryszard, et al. "Quantum entanglement." Reviews of modern physics 81.2 (2009): 865-942.

[32] Andreas, Andreou, et al. "Quantum Computing in Semantic Communications: Overcoming Optimization Challenges With High-Dimensional Hilbert Spaces." IEEE Access (2025).

[33] Sarwar, Muhammad Saood, and Shahzaib Ur Rehman. "Hybrid quantum-classical machine learning for enhanced PCOS classification." Quantum Machine Intelligence 7.2 (2025): 83.

[34] Tomar, Sahil, Rajeshwar Tripathi, and Sandeep Kumar. "Comprehensive survey of qml: from data analysis to algorithmic advancements." arXiv preprint arXiv:2501.09528 (2025).

[35] Khan, Tariq M., and Antonio Robles-Kelly. "Machine learning: Quantum vs classical." IEEE Access 8 (2020): 219275-219294.

[36] T. Reimer, J. Krenkevich and S. Pistorius, "An Open-Access Experimental Dataset for Breast Microwave Imaging," 2020 14th European Conference on Antennas and Propagation (EuCAP), Copenhagen, Denmark, 2020, pp. 1-5, doi: 10.23919/EuCAP48036.2020.9135659.

[37] H. Shadwell et al., "Machine Learning Techniques for Autonomous Lesion Detection in Microwave Breast Imaging Clinical Data," 2024 18th International Symposium on Medical Information and Communication Technology (ISMICT), London, United Kingdom, 2024, pp. 95-98, doi: 10.1109/ISMICT61996.2024.10738019.

[38] Janjic, Aleksandar, et al. "Microwave breast lesion classification–results from clinical investigation of the safe microwave breast cancer system." Academic radiology 30 (2023): S1-S8.

[39] T. Reimer and S. Pistorius, "The Diagnostic Performance of Machine Learning in Breast Microwave Sensing on an Experimental Dataset," in IEEE Journal of Electromagnetics, RF and Microwaves in Medicine and Biology, vol. 6, no. 1, pp. 139-145, March 2022, doi: 10.1109/JERM.2021.3076100.

[40] Rana, Soumya Prakash, et al. "Radiation-free microwave technology for breast lesion detection using supervised machine learning model." Tomography 9.1 (2023): 105-129.

[41] RV, Aswiga, Sridevi S, and Indira B. "Leveraging quantum kernel support vector machine for breast cancer diagnosis from digital breast tomosynthesis images." Quantum Machine Intelligence 6.2 (2024): 40.

[42] Liu, Yu-Ting, et al. "Weighted fuzzy Dempster–Shafer framework for multimodal information integration." IEEE Transactions on Fuzzy Systems 26.1 (2017): 338-352.

[43] Chowa, Sadia Sultana, et al. "Graph neural network-based breast cancer diagnosis using ultrasound images with optimized graph construction integrating the medically significant features." Journal of Cancer Research and Clinical Oncology 149.20 (2023): 18039-18064.

[44] A. Oskooi, D. Roundy, M. Ibanescu, P. Bermel, J.D. Joannopoulos, and S.G. Johnson, "MEEP: A flexible free-software package for electromagnetic simulations by the FDTD method," Computer Physics Communications, Vol. 181, pp. 687-702 (2010) (pdf).

[45] Davis, Jeffrey A., et al. "Encoding amplitude information onto phase-only filters." Applied optics 38.23 (1999): 5004-5013.

[46] Hearst, Marti A., et al. "Support vector machines." IEEE Intelligent Systems and their applications 13.4 (1998): 18-28.

[47] Liu, Quanzhong, et al. "Feature selection for support vector machines with RBF kernel." Artificial Intelligence Review 36.2 (2011): 99-115.

[48] Innan, Nouhaila, et al. "Enhancing quantum support vector machines through variational kernel training: N. INNAN et al." Quantum Information Processing 22.10 (2023): 374.

[49] Dian Arif, Rachman, and Akrom Muhamad. "Variational Quantum Circuits Design Principles, Applications, and Challenges Toward Practical: A Review." Journal of Multiscale Materials Informatics 2.2 (2025): 16-29.